Manusscript: 329606

Title: Numerical studies on radiative heat loads to plasma facing components for the W-7X stellarator

First Author: T.Eich, Max-Planck-Institut für Plasmaphysik, EURATOM Association, Boltzmannstr. 2, D-85748 Garching, Germany

Second Author: A.Werner, Max-Planck-Institut für Plasmaphysik, EURATOM Association, Wendelsteinstrasse 1, D-17491 Greifswald, Germany

Corresponding Author: T.Eich, Email: thomas.eich@ipp.mpg.de, Telephone: +49-89-3299-1927, Fax: +49-89-3299-1812

Number of Pages: 57

Number of Tables: 3

Number of Figures: 19

No color figure in printed version, only in online version ('Color Online')

Keywords: stellarator, radiative heat load, monte-carlo-simulation

Numerical studies on radiative heat loads to plasma facing components for the W-7X stellarator

T.Eich and A.Werner

Abstract. The heat load due to plasma radiation is estimated for the plasma wall components of the stellarator Wendelstein-7X (W-7X). A fully 3D Monte-Carlo code is used to simulate heating of first wall components due to photon emission from the plasma. The plasma wall components can be described in a complex way with arbitrary shapes, orientation and flexible numerical representation. The volume radiation distribution is assumed to be described by poloidal symmetric and radially varying 1-D profiles aligned to the magnetic flux surfaces. A further example is given by a non poloidal symmetric radiation distribution following the 5 X-Point regions of the island divertor magnetic structure. Several realistic and artificial radiation profiles are chosen to investigate the local heat loads on an idealised plasma wall. The first detailed technical application of the code is the estimation of the local heat load on the Thomson-scattering windows and onto the inner surface of several vacuum ports of one half module of the W7-X plasma vessel.

1. Introduction

The Wendelstein-7X (W7-X) experiment is a stellarator with super conducting coils which should permit plasma duration of up to 30 minutes with heating powers of about 10MW in steady-state operation by electron cyclotron resonance heating (ECRH). Additional neutral beam injection (NBI) and ion cyclotron resonance heating (ICRH) can be applied to reach heating levels up to 19MW for duration of about ten seconds[1]. The main fraction of the heating power is expected to be transported either convectively to the divertor target plates or by plasma radiation towards the plasma wall.

In the Wendelstein 7-AS (W7-AS) stellarator island divertor configuration [2] and in currently operating tokamak experiments, see e.g. JET and ASDEX Upgrade, the power loads to the plasma facing components (PFC) have been extensively studied. The highest heat loads are deposited on the target tiles in the divertor [3]. Due to the (relatively) short discharge durations of less than 10 seconds with heating powers of about 5-20MW, the thermal inertial mass is sufficient to avoid overheating of these tiles, which is defined by an anticipated sublimation temperature of 2300^oC for carbon tiles. The peak heat fluxes are measured to be in the range of $10\mathrm{MWm}^{-2}$ for JET and ASDEX Upgrade on the divertor target plates. A similar value is expected for W-7X divertor target tiles[4]. The radiation heat load on the divertor target plates can be neglected, since the plasma heat flux load is expected to be two orders of magnitude larger.

The radiation heat loads on the main fraction of the inner wall due to plasma radiation and charge exchanges (CXR) neutral particles are not a serious problem in current devices except for effects of physical and chemical sputtering [5]. A steady-state experiment like W7-X imposes the demand for actively cooled first wall components

including plasma or radiation exposed diagnostics

Most of the in-vessel area is covered by panels, which are actively cooled and capable of handling a power load of $100\frac{kW}{m^2}$ in steady state operation. Particularly the specially designed parts of diagnostically systems, their edges and the welding joints of about 300 ports in W-7X are potentially affected by radiation heat load.

Due to the complex 3D geometry of the magnetic flux surfaces even a smooth radially varying radiation profile, e.g. monotonically decreasing with small radius a, generates a complex and non homogenous radiation pattern on the inner wall. For each port or diagnostic, the local heat load has to be estimated individually due to the large variety in the ports and diagnostics orientation and locations.

For this reason a full 3D Monte-Carlo code has been developed, which is able to calculate the local heat load on arbitrarily oriented and shaped in-vessel components generated by a radiation profile aligned to e.g. the magnetic flux surfaces, but also any other numerically given three dimensional radiation distribution can be used. The numerical representation of the complex in-vessel, diagnostic and port geometry is fully compatible to the ANSYS [6] finite element method (FEM) based solver package to allow (i) usage of the CAD data and (ii) calculation of temperature distribution and resulting thermal stresses in a later step which is not included in this work. Also, this paper will not assess the cooling capacities of the in-vessel components based on the current active or passive cooling machine design. The components specially designed to bear the large convective heat load carried by the plasma flowing along open magnetic field in the so called scrape-off-layer region, i.e. the divertor target plates, are not considered in this paper. Nevertheless, their positions are marked in Figure 3.

A self consistent description of the plasma equilibrium, resulting edge plasma

transport to the divertor and first wall areas, e.g. as aimed in sophisticated edge plasma transport codes for W-7X, e.g. [7] or [8], and potentially coupled to a combined neutral particle/photon transport code, e.g. EIRENE [9], is beyond the scope of the paper.

2. Visualisation of the 3D geometries and technical considerations on data processing

The 3D visualisation of the magnetic fields, radiation profiles and finally heat fluxes and the plasma wall is non trivial due to the complex 3D shape of the magnetic fields, the resulting radiation profiles and particularly the highly complex structure of diagnostics and thus deserves detailed consideration as given in this section.

2.1. Areas of interest for this paper

In this work we distinguish three different parts of of the inner wall.

First there are divertor target plates which are optimised for high heat fluxes (HHF-components). These areas receive nearly the full convective heat load as shown for the Wendelstein-7 AS stellarator experiment using the island divertor concept[10]. The additional heat load due to radiation can be neglected for the HHF components. Even cases with extremely large local radiation in front of the divertor target plates like under detached plasma conditions as observed in tokamaks in impurity seeded discharges[11] will only impose marginally higher local heat fluxes to the HHF-components, since then the fraction of convective heat load is strongly reduced. However, an intense poloidally asymmetric radiation distribution aligned e.g. to the (helically varying) X-point regions, as observed e.g. for the Wendelstein-7 AS stellarator[12][13], imposes increased radiation heat fluxes to the divertor baffle structures, which are designed to receive $500\frac{kW}{m^2}$ heat load. To assess these heat loads the current stage of the Monte-Carlo code for photon

tracing does not include such asymmetries and will be addressed in a later step of model development.

Secondly we have to consider the plasma wall which is covered by steel panels backed by water cooling pipes and being able to remove heat loads of $100\frac{kW}{m^2}$ in the quasi steady state operation of 30 minutes.

Finally we will consider individual exposed parts of diagnostics and the differently shaped ports, in which they are embedded. Since a detailed description of all diagnostics aimed for the start-up phase of the W7-X project is too complex and time consuming, we focus on the example of the Thomson-scattering system to have a reference case for later considerations as presented in section 4.4. However, a complete estimation of all important quantities (within the aimed goals of the paper) for each port in one half module is given.

2.2. Numerical procedure

The simulation of the photon fluxes in advanced stellarators required the development of a new code LOWENDEL (Loads on Wendelstein). Although the basic numerical procedure is fairly simple, that is starting simulation photons according to a given distribution on flux surfaces and tracing them to their intersection with the wall components, the execution in the complexly shaped plasma and wall geometry is non-trivial. The main reason for a new development is the insufficient representation of the limiting vessel structures, in particular when ports are taken into account. Quite often, the wall representation for simulation codes is based on poloidal cross sections, in which the boundary is represented by polygons.

For the present simulation the main ingredients are the representation of the plasma geometry, e.g. based on Fourier representation of the main flux surfaces, and the

representation of the wall components with a convenient interface to CAD systems. The simulation procedure is as follows:

- The geometrical data of the wall components are transferred from the CAD system to the commercial finite element solver tool ANSYS. The surfaces are meshed using surface elements based on 3 nodes $\vec{N}_i$ (triangles) with the shape function

$$\vec{x} = \frac{1}{2}\left[(1-s)\vec{N}_0 + (s+t)\vec{N}_1 + (1-t)\vec{N}_2\right] \tag{1}$$

$$with \quad -1 \leq s,t \leq 1 \quad \wedge \quad s+t \leq 1 \tag{2}$$

  with s,t being the parameters to span the finite element surfaces and simultaneously non-planar quadrilateral elements given by

$$\vec{x} = \frac{1}{4}\left[(1-s)(1-t)\vec{N}_0 + (1+s)(1-t)\vec{N}_1 \right. \tag{3}$$

$$\left. +(1-s)(1+t)\vec{N}_2 + (1-s)(1+t)\vec{N}_3\right] \tag{4}$$

$$with \quad -1 \leq s,t \leq 1 \tag{5}$$

  The mesh data is transferred to the simulation code, in which a spatial hash table is generated for the position of the basic surface elements allowing fast intersection calculations. The interconnection between these surface primitives is given by the node-element representation. Note that in the current version of the code the surface primitives are the surfaces of simple finite elements only. More complex surface primitives can in general be used for the representation of the vessel structure, but are not realised so far in the code.

- Next, the representation of magnetic surfaces is generated. The magnetic field data can be created using a filament approximation of the coil geometry and Biot-Savart's formula or the more sophisticated MFBE calculations [14], which are based on MHD equilibrium calculations of finite beta plasmas. The code searches

Separatrix (X-Point) locations in order to separate the edge from the inner surface topology and calculates the Fourier representation of the inner part by field line tracing.

- The test photons are launched from surfaces according to the 1D profile $\sigma(\rho)$ of the radiated power per volume. With the assumption that the emission profile is a flux quantity, the emission probability is calculated by

$$dp(\rho) = \sigma(\rho) d^3 r \tag{6}$$

$$= \sigma(\rho) \left(\vec{\nabla}\rho \cdot \vec{\nabla}\vartheta \times \vec{\nabla}\varphi \right)^{-1} d\rho d\vartheta d\varphi \tag{7}$$

with ϑ being the poloidal and φ the toroidal angular variable in flux coordinates. The launched photons are traced until there trajectory intersects one of the surface primitives or leaves the computation region, with is a toroidal enclosure defined by the surfaces primitives of the vessel wall components. Although the photon trajectory is a straight line, the procedure solves an (trivial) equation of motion for the photons numerically, with a step size being smaller than the mesh with of the hash table, which stores lists of the surface primitives in the close proximity. Using this approach, the equation of motion can be easily replaced by others, e.g. for field line or particle tracing. Due to this, a numerical procedure for estimating the convective loads by field line diffusion [15] could be already easily implemented. It should be stressed that the determination of the strike points does not require a logic separating the volume in an inner and outer region as in former codes [14].

- Each test photon carries some power which is attributed to the surface primitive it strikes. This power can be averaged per surface primitive or per node and divided by the corresponding area. In case of nodal averaging, one has to define area of the vicinity of the node counting to the area and the power load. Finally, the result

is stored in shape functions, e.g. for the quadrilateral the heat flux on one surface primitive is given by

$$Q(s,t) = \frac{1}{4}\left[(1-s)(1-t)Q_0 + (1+s)(1-t)Q_1\right. \tag{8}$$

$$\left.+(1-s)(1+t)Q_2 + (1+s)(1+t)Q_3\right] \tag{9}$$

with Q_i being the heat flux determined for node $\vec{N}_i$. Taking all surface primitives, the result is a heat flux distribution on the component surfaces, which can be transferred as a boundary condition to the ANSYS finite element solver for thermal analysis. The mesh used the further analysis may differ from the mesh used for the simulation. The heat loads can be interpolated to any points being close enough to the surface primitives by searching the point of closest approach over all surface primitives in the vicinity and transferring $Q(s_{min}, t_{min})$.

Of course, the local heat load values established by a distribution of single energy packages (or photons) has some statistical noise. In the present state of the code, no advanced procedures for statistic improvements have been developed, but basically two options are envisaged for further implementation. Firstly, one can define some components of interests. In the toroidal region around this component more photons could be launched having some lower statistical weight. The second option is to perform back tracing of photons from surfaces being under investigation. This option is necessary for analysis of small structures like some parts of diagnostics, which must be represented by surfaces primitives having tiny areas. In addition to launching more flights near an in-vessel component, flight splitting could be considered to be used in future versions of the code to describe photon scattering events, such as absorption and reemission in optically thick media.

2.3. Magnetic vacuum field

The standard magnetic field of the W-7X is given by a coil current distribution as described in table 1. For the visualisation of the magnetic field we chose Poincaré-plots as shown in Figure 2, which describe the magnetic field by a set of representative field lines. The intersection points of each field line with a reference plane is marked; this way the 3D structure of the magnetic field is represented by a set of 2D planes. For this paper we have chosen a set of 4 planes representing one half module with a toroidal extension of $2\pi/10$ defined by $\Phi_{tor.}$ =0,$\pi/15$,$\pi/10$ and $\pi/5$. The planes in the other part of the half module with negative $\Phi_{tor.}$, namely 0,$-\pi/15$,$-\pi/10$ and $-\pi/5$ are not shown since they are simply inverted with respect to the planes with positive $\Phi_{tor.}$. This way also island structures or ergodic regions, i.e. region which cannot be described by flux surfaces, are illustratively visualised[16]. Ergodic structures outside the LCFS are not shown. The field lines outside the LCFS impose a region with laminar transport properties and are characterised by short connection lengths [17][18][19].

2.4. Un-winding of the plasma wall

The plasma wall for W7-X is represented by transforming each point of the plasma wall onto a reference plane using a numerical un-winding procedure. This un-winding is chosen for convenience and not unique, other options may have advantages depending on the exact considerations. The transformation of the Cartesian coordinates x,y,z towards the un-winded 2D reference plane is given next. First we use the standard polar coordinates R_{polar}, Φ_{polar}, z given as

$$R_{polar} = \sqrt{x^2 + y^2}$$

$$\Phi_{polar} = \arctan(y/x)$$

$$z_{polar} = z$$

A reference axis is defined by a numerical expression (given in mm) such as

$$R_{axis} = 5555.6 + 373.2 \cdot \cos(5\Phi_{polar}) + 16.1 \cdot \cos(10\Phi_{polar}) + 1.15 \cdot \cos(15\Phi_{polar}) \quad (10)$$

$$z_{axis} = 309.3 \cdot \sin(5\Phi_{polar}) + 18.7 \cdot \sin(10\Phi_{polar}) + 0.3 \sin(15\Phi_{polar}). \quad (11)$$

Relative to this axis each point on the wall is described with the two angles $\Theta_{\oslash}$ and $\Phi_{\oslash}$ and a distance to the wall elements $r_{\oslash}$.

$$\Phi_{\oslash} = \Phi_{polar}$$

$$\Theta_{\oslash} = \arg\left(R_{polar} - R_{axis} + i \cdot (z_{polar} - z_{axis})\right)$$

$$r_{\oslash} = \sqrt{(R_{polar} - R_{axis})^2 + (z_{polar} - z_{axis})^2}$$

At this point it useful for the later interpretation to show the exact dependence of $r_{\oslash}$ on $\Theta_{\oslash}$ and $\Phi_{\oslash}$.

2.5. Distance of the plasma axis to the plasma wall

In figure 3, the distance between the plasma axis at $\rho = 0$ and the plasma wall is illustrated. The distance,$r_{\oslash}$, varies largely between 0.3m and 1.4m and shows a characteristic pattern resembling the five-fold symmetry of the W-7X magnetic configuration. Particularly the outer midplane region in the bean plane ($\Phi = 0$, $\Theta = 0$) and the inner midplane region in the bean plane ($\Phi = 0$, $\Theta = \pm\pi$) shows a short distance to the plasma axis when compared to the top and bottom locations ($\Phi = 0$, $\Theta = \pm\pi/2$) of the plasma vessel. For the triangle plane at $\Phi = \pm\pi/5$ the variation is also existing but less pronounced. Areas with small $r_{\oslash}$ values will be in the focus of the considerations on the maximum local heat fluxes. Furthermore we are able to identify the regions with large and small variations of the $r_{\oslash}$ value (mainly in poloidal direction)

which will be in the main focus when looking for the maximum gradients of the local heat fluxes.

2.6. Mesh width and statistical requirements

The code uses a Monte-Carlo method to estimate the local heat fluxes on the plasma wall and port structures including diagnostical features. We will discuss now the number of test photons that have to be traced so that each individual area of interest is described accurately enough.

- *Local heat fluxes on the closed (idealised) plasma wall:* The closed (idealised) plasma vessel wall is represented by a grid of 250 toroidal times 60 poloidal mesh points resulting in 15000 subareas. Each subarea has roughly a size of 0.13m^2. The numerical description of the ideal plasma wall assumes a toroidally closed set of differently shaped boundaries (as shown in figure 2) of the plasma vessel with a constant toroidal distance of 4.5^o between each boundary.

  As mentioned before the numerical method for the photon tracing is a Monte-Carlo method. Therefore, the time consumption for the calculation increases linearly with the number of started photons. To reach an amount of $5 \cdot 10^7$ photons the program needs about 4 hours using a standard PC with 2GB memory and 1GHz . It turned out that this number of photons provides a good trade-off between statistical errors and calculation time and memory consumption. Since the idealised plasma vessel wall can be described by a comparably small number of single grid elements, the statistical error is negligible compared to the deviations introduced by an idealised numerical description using MatLab©. The statistical error (after averaging the result of the 5 identical modules to one module) is less than 1%. An important fact at this point is that each calculated photon contributes to the overall result, since

each photon hits an area of interest. Note, that each photon is started toroidally and poloidally uniformly from the whole plasma volume.

- *Local heat fluxes on special in-vessel components:* For the assessment of the cooling capability for particular components or the port structure, the real 3D numerical representation of those components is read out from the CAD system and read into the ANSYS© FEM solver package software. A highly flexible triangulation is performed which can already be optimised for the requirements of the Monte-Carlo solver package. As a general concept, the finite element grid size is chosen so that the most likely element edge has a maximum length of about 20mm. An optimised finite element grid for the purpose of local heat transport in the component structure or for an expansion due to thermally induced stresses inside the machine structure cannot be estimated. It is very likely that such an estimation requires an interactive exchange of data between the Monte-Carlo solver using adapted mesh widths and the ANSYS solver package calculating the thermal conduction or stress induced expansions. An important point for the calculation of local heat flux is that most photon do not hit the areas of interest but hit other parts of the machine. For this reason the calculation times are much larger and result in weak statistics for the most remote parts of the considered structures. Many of the finite elements describing the most remote areas e.g. at the end of very long ports with a small opening (like the AEX port, which is extensively studied in section 4.2) do not receive enough photons to have sufficient statistics for each element.

  A possible way to escape this general problem is to trace photons backwards from these small and remote areas and to calculate the line integral of photon through the entire plasma volume weighted by the strength of the radiation source as already

pointed out.

3. Radiation heat loads

In this section we first discuss the heat impact of an *artificial* plasma radiation distribution on the wall to understand the effect of the geometry on the resulting heat load patterns. This will be done for three different cases (1-3). Then we will discuss the results obtained by two realistic radiation profiles, cases (4-5).

It is assumed that all photons reaching any element will be absorbed without reflection, which is well justified for photon energies larger than $10eV$. Details about the dependence of the reflection coefficient on the photon energy and incident angle can be found in [20]. Improvements on this assumption, particular for large iron surfaces inside the ports are possible for a later stage of the model development. We will therefore not distinguish between the different nature of the photon sources and resulting wavelengths depending on the assumption of plasma radiation scenarios nor the different wavelength depending reflectivity of the in-vessel components made of e.g. carbon or iron. In Figure 4 the five cases are illustrated which will be used in this paper to study the effects of radiation heat load. Cases (1,2,3) are artificial profiles. They represent a radiation sources (1) in the central plasma ($\sigma(\rho) = 1$ for $0.0 \leq \rho \leq 0.1$), (2) half way radially out ($\sigma(\rho) = 1$ for $0.45 \leq \rho \leq 0.55$) and (3) in the edge plasma ($\sigma(\rho) = 1$ for $0.9 \leq \rho \leq 1.0$), where $\sigma(\rho)$ (see Eqn.6) is the radiated power per volume normalised in such a way, that the whole plasma volumes radiates a power of 10MW (also true for cases (4,5)). These three artificial profiles are used to understand the impact of the radiation source centred around the magnetic flux surfaces at different radii.

The two cases (4,5) in Figure 4 are assumed to represent realistic radiation profiles

in the experimental campaign of W-7X. Also here both cases are normalised to 10MW radiated power. Case (4) describes emission proportional to the square of the minor radius and thus most of the power is radiated from the core region. Case (5) describes emission proportional to the square of the minor radius as in case (4) but with additional line radiation from impurities in the very edge region. The radiation distribution described in case (5) is chosen in such a way that both the fraction of radiated power with an identical radial dependence as in case (4) and the fraction of radiated power due to the line radiation at the very edge are 5MW.

Since the results have an exact linear dependence on the latter value, heat loads resulting from a lower or higher radiated power can be easily obtained from the presented results. It should be noted that an amount of core radiation in the order of 10MW is very high and is not expected in steady operation. Results from case (4) thus may be adjusted to lower core radiation values.

The case (5) describes a situation of either a high impurity content in the edge region achieved e.g. by impurity seeding or a high density edge region like in the HDH-Mode[21, 22, 23] or a combination of both. In both latter cases a high level of line radiation from the edge was achieved as reported from Wendelstein-7 AS experiments[24]. Enhanced edge radiation has also been in the focus of detailed studies for tokamak power handling experiments like e.g. JET [25] or ASDEX Upgrade [26].

In contrast to case (4), case (5) is assumed to describe a realistic absolute amount of radiated power also in steady operation. Due to the presence of impurities, seeded or intrinsic, also the core radiation is assumed to exceed the amount of radiation achieved with pure deuterium bremsstrahlung. Finally, it should be noted that all presented studies do only describe situations of poloidally symmetric radiation sources. One

example case of a non poloidal symmetric radiation source, as given in the case of X-point radiators observed in the W7-AS experiment[27] [28], will be presented in chapter 5.

3.1. Results for the idealised plasma wall

In Figure 5 the local heat flux density on the idealised plasma wall is shown for a centrally peaked plasma radiation source (case (1)). As it can be seen, the heat flux pattern is non homogeneous and reflects the helicity of the plasma vessel and magnetic field. The maximum and minimum local heat fluxes vary by about a factor of 13. The largest local heat fluxes are existent at the outer ($\Phi_\oslash$ =0, $\Theta_\oslash$ =0) and inner ($\Phi_\oslash$ =0, $\Theta_\oslash$ =$\pm\pi$) equatorial midplane in the bean plane. The smallest heat fluxes are at the top and bottom of the plasma vessel, since the distance to the plasma axis is largest at this location.

The two smaller figures at the right of the large figure display the local heat flux density at five cuts in direction of $\Theta_\oslash$ and in direction of $\Phi_\oslash$. The sufficient amount of traced photons can be verified by comparing e.g. the cuts at $\Theta_\oslash = \pm\pi/2$ or e.g. $\Phi_\oslash = \pm\pi/10$, which are nearly mirror imaged.

In Figure 6 and 7 the local heat flux density on the idealised plasma wall is shown for the case (2) and (3), respectively. The variation of the local heat flux density is less pronounced as compared to case (1) and the peaking factor, the difference between the maximum and minimum heat flux density value, is about seven for case (2) and down to three for case (3); for case (1) it is about 13. The largest local heat fluxes are shifted towards the triangle plane ($\approx \Phi_\oslash = \pm 1/10\pi$) and towards the inner equatorial midplane position of the plasma vessel ($\approx \Theta_\oslash = \pm 1/2\pi$) in both cases. Identical to case (1), the regions of the minimum local heat flux are the top and bottom part of the plasma

vessel. It should be noted, that the results for case (2) shows values which lay always between the results for case (1) and case (3). This behaviour has also been checked for further artifical cases (which are not shown here) with the step function like radiation distribution shifted in even smaller steps ($\sigma(\rho) = 1$ for ρ=0.1-0.2,0.2-0.3,0.3-0.4 etc.) where the same result has been found.

As an important and very basic result it should be worth notifying, that the heat load distribution on the first wall depends strongly on the radial position of the power radiation, which is a basic difference to tokamaks. This is because in contrast to the situation in W-7X in a tokamak the poloidal dependence of the minimum distance between a closed flux surface and the first wall is only slightly varying with the minor radius. Also, the regions of maximum peak heat load are poloidally and also toroidally varying, although the volume radiation strength is both, poloidally and toroidally constant on flux surfaces. Going from a more centred radiation profile as approximated in case (1) radially out as performed in case (2) and finally describing a pure edge radiation as in case (3), the regions of peak heat load get shifted and the peaking factor decreases significantly. The reason for the decrement of the peaking factor by the radial shift of the radiation, is that the variation of the minimum distance between the flux surfaces at the very edge and the first wall is smaller than the variation of the minimum distance between the flux surfaces in the core region and the first wall, as it can be verified in Figure 2.

Here it is most important to note, that a radiation distribution with the maximum volume radiation at the edge imposes indeed a smaller peaking factor than a centred radiation distribution which is a favourable result for the applicability of seeding techniques for Wendelstein-7X.

Figure 8 shows the results of the heat load due to radiation based on the assumptions for the realistic case (5). As it can be seen in the plot, the regions of maximum heat flux are first in the top left and bottom right corner of the plot showing values of around 60 $\frac{kW}{m^2}$, identical to the case (3). A second region of maximum heat flux can be observed in the exact middle of the plot with values around $50\frac{kW}{m^2}$, with an identical position of this local maximum to case (1). Since the peak value of $60\frac{kW}{m^2}$ representing the influence of a large edge radiator, and the peak value of $50\frac{kW}{m^2}$ arising from a parabolic radiation distribution are roughly equal, we conclude in return that a radiation distribution similar to case (5) is close to an optimised realistic radiation distribution in the sense of avoiding large peak heat loads. If such a radiation distribution, namely a poloidal symmetric large edge radiator can be realised (see in that respect chapter 5) needs to be adressed experimentally or with sophisticated edge codes.

Finally we present in Figure 9 the difference, Σ, between a linear approximation of case (5) and the calculated values for case (5) following the simple expression:

$$\Sigma(\Phi_{\oslash}, \Theta_{\oslash}) = \frac{0.20 \cdot q_{Case(1)} + 0.17 \cdot q_{Case(2)} + 1.0 \cdot q_{Case(3)}}{0.20 + 0.17 + 1.0} - q_{Case(5)}$$

The weights for the linear approximation (0.20,0.17 and 1.0) are derived simply by taking the value of $\sigma(\rho)$ at the the position $\rho = 0.05$, 0.50 and 0.9 for the cases (1,2,3), respectively. As it is shown in the Figure 9, the accuracy of the linear approximation is reasonable; the maximum/minimum value for Σ is about $\pm$ 15%, respectively. Based on the latter result, as well as the results presented in the next chapter, it appears to be useful to take a linear combination of the cases (1,2,3) in order to get a quick and simple estimate for other radiation distributions of interest, such as cases with e.g. a larger fraction of edge radiation and complementary a lower core radiation fraction.

3.2. CXR particle transport simulation

Besides the plasma radiation the CXR particles will also contribute to the local PFC heat fluxes. They are generated by the interaction between low energy neutral particles released from the wall elements entering the plasma and high energetic ions by exchanging an electron, so that after the charge exchange collision the neutral particle is highly energetic and travels quickly again towards the plasma wall elements. This CXR process can lead to significant power loading on the plasma wall in case e.g. of a high edge density. The neutral particles leave the magnetic confinement region just as the photons. We assume therefore, that the CXR power load can be simulated as the photon transport when considering the pure thermal heat load and not e.g. physical material sputtering. All presented calculations are normalised to 10MW radiated power, and we assume that the whole CXR fraction of power to the wall elements is included in that number without being able to quote an exact value for the CXR radiation fraction. In case that the CXR fraction does significantly increase the overall power load to the wall, the results just need to be linearly scaled to the corresponding value.

3.3. High energetic ions orbits losses towards the plasma wall

High energetic ions with energies covering 10keV to 100keV, generated e.g. by NBI and ICRH CXR processes, can be so fast that orbits significantly differ from the magnetic field lines in such a way, that they do not hit the divertor target plates but other parts of the first wall. Their orbits mainly hit the divertor target areas but will also contribute to the local heat loads on the PFC areas. For Wendelstein-7X these additional local heat fluxes were estimated [29] for the case of high mirror fields (increased field strength in the bean shaped cross section). This particular configuration was chosen since in this

case the fraction of fast particle losses compared to other foreseen magnetic equilibrium fields for the operation of W7-X is smallest, for details see [29]. The total amount of fast particles escaping to plasma wall is about 50kW, less than 1% of the expected radiated heat load. Detailed investigations have to be carried out to estimate the resulting local heat flux densities from the fast particles power of 50kW, since they could cause so called *hot spots* as observed e.g. in ASDEX Upgrade in NBI heated high triangularity plasmas [30]. Influences of the energy spectrum on these fast particles and the resulting physical sputtering yields [5] (on low or high Z materials) should be considered as well. However, both issues are beyond the scope of the paper.

4. Applications

In the following section some applications of the code will be presented to show (a) the flexibility of the code and (b) give an impression on the actual detailed solution which is necessary to design a fusion experiment with up to 30 minutes plasma duration at 10MW heating power.

4.1. Heat fluxes at the port openings locations

An important aspect for the design of cooling panels for the port is the local heat flux onto the inner surface of the ports. Additionally, information is required about the overall power impact on the entire inner port wall and the port top cover plate, since the cooling water capabilities must be designed to remove the power loadings completely after each discharge and also to maintain a reasonable temperature during the discharge.

In Figure 10 an overview is given of the plasma wall and the 34 ports that have been foreseen for heating, supply and diagnosing the magnetically confined plasma (see also Figures 1 and 2). For each of the 34 ports as drawn in the figure and the plasma

wall a numerical mesh is generated, which contains 200-2500 finite elements per port. As done for the idealised inner wall, all photons per finite elements are counted and a local heat flux density is calculated taking the number of photons times their energy and dividing by the area of the finite elements.

In Figure 11 the local heat flux distribution onto the idealised inner wall is given for the radiation profile of case (5) allowing recognition of the ports opening. Case (5) is chosen, since this case is expected to be that scenario with the largest absolute amount of radiated power due to the presence of seeded impurities in the edge. For a subset of ports we have indicated the port construction design names which are used throughout the paper and have been used already in Figure 10. We estimate the local heat flux densities normal to the port openings $q_\perp$ as they can be verified in the Figure and summarise them in Table 2. In Figure 10 also the opening of all other ports can be verified which are not discussed explicitly. This procedure is also applied to the other cases (1-4).

To benchmark the numerical results for the heat load onto the inner port walls, we will present in section 4.3 an analytical model for the heat flux density distribution for the ports. As an input for this model we use the also estimated $q_\perp$ value as the heat flux density normal to the port axis as it will be discussed in detail in section 4.3.

4.2. Heat load distribution inside port structures

The important positions for the cooling requirements of single ports are illustrated in Figure 12. Along the port axis R, four distances from the port entrance along the port axis are chosen to assess the required cooling capacity for each port, namely at R_1=0cm,R_2=20cm,R_3=20cm+50cm=70cm and at R_4 which is the transition location from the solid port structure to the necessarily flexible and therefore thin bellows which

is different for each port and therefore no number for the distance is given. The cooling capacity is in return given by the heat conduction of the clamping connecting the port inner wall with the water pipes at the rear side of each port wall. Again, it should be noted that it is not the aim of the paper to assess the required cooling capacity but to provide the incoming local heat fluxes at the positions Pos.1-4 at R_1,R_2,R_3 and R_4

The most critical positions are at the port opening (Pos.1) and at the transition to the bellows (Pos.4). At the latter position the cooling capacity is critical, since it is very difficult to remove heat from the bellows as no solid clamps or fixing can be mounted between the rigid water pipes and the bellows. The bellows themselves are not included in the numerical model since their numerical representation is too complex and because their exact location and orientation will vary during the discharge due to the expected differential movements of the inner and outer vessel[1]. The essential information provided by the presented numerical modelling is the maximum local heat at the bellow entrance and the information that the local heat flux will further decay when going along the port axis. The port wall at Pos. 1 will receive the largest heat fluxes and will need maximum cooling capacities there. Positions 2 and 3 are chosen since at their locations the water cooling efficiency is reduced due to engineering restrictions. For details see [31].

In Figure 13 is the result of the numerical calculation and an analytical calculation for the radiation heat load onto the inner port surface of the port AEX is presented. Numerically, a line is assumed in the centre inside the ports. Each point on this axis a is gained by averaging all local heat flux values of single elements which are located in a certain acceptance angle normal to the port axis. The red points in the left picture denote e.g. the acceptance range of 90^o $\pm 12^o$. The data points for two additional

acceptance angles of 4 and 8^o are subsets of the red data points and not shown explicitly. The numbers of 12^o , 8^o and 4^o degrees are chosen to provide a reasonable statistic of single data points and correspond to a maximum distance of two neighbouring data points along the port axis R of $\approx$ 2cm.

From these three sets of data points three heat load values are gained by averaging all values within the divergence of 90^o $\pm$4,8,12^o for each point of the port axis a. The error bars of the numerical result take the standard deviation of each data set (4,8,12^o) and between the mean values of the data sets into account. In addition to the four positions along the port axis defining the subareas of different cooling capacity ($q_{P1,P2,P3,P4}$) the values of radiative heat flux on the top cover (q_{cover}) as well as the total power on the wall (P_{port}) and the top cover P_{cover} are given.

For the port AEX we find from Figure 11 a heat flux density normal to the port opening of $q_\perp$=49.3$\frac{kW}{m^2}$. From Figure 13 we see that the maximum local heat flux onto the inner port at $a = 0m$ is q_{P1}=24.4 $\frac{kW}{m^2}$. This is the value when averaging all values within the introduced acceptance ranges. When going to larger values of a, deeper in the port away from the plasma axis, the local heat flux onto the wall decays and we can mark the positions and values for q_{P1} - q_{P4}. A further important aspect is the scatter within the finite elements around the Pos.1 ($a = 0m$), since some elements receive a much larger local heat flux than the average of the data set. This is not due to a statistical scatter but reflects the real complex 3D geometry of the port structures depending on the exact port orientation and location. For this reason we also give for each port the value q_{P1}^{max} which is the average of the three finite-elements with the largest local heat fluxes at the position Pos.1 ($a = 0m$). To avoid numerical errors only such finite-elements are used which have a minimum area of $A = 2.0cm \times 2.0cm$.

In Figure 14 the same information is given for the port AEE. This port is located at the outer equatorial midplane and has a rectangular cross section with the largest port opening (together with the port AEA) of all ports for the W-7X stellarator. Again, it can be seen that the q_{P1} value is roughly the half of the $q_{\perp}$ value for the port location and that the local heat fluxes decay monotonically with larger a.

This procedure is repeated for all 34 ports and all values are summarised in the Table 2. Additionally, the results of the analytical model for the ports AEX,AEE and AEA are given.

4.3. Comparison to an analytical model

To benchmark the numerical results with an analytical model we now calculate the power flux densities onto the port inner surfaces for a tube with circular cross section and radius r_{port}. To avoid further difficulties introduced by the different orientations of the port openings relative to the plasma axis, which is in general not in line with the idealised wall, we take the port AEX (see figure 10 and figure 13) since for this port the opening is aligned normal to the idealised plasma wall. From the calculation as done in section 3.1 and summarised in tabular 2, we use an average normal power flux density into the port structure of $q_{entr.} = q_{\perp}$ =49.3$\frac{kW}{m^2}$.

Figure 15 illustrates how the power flux densities are calculated. The power flux density normal to the port axis a is given by

$$q_{\perp}(a) = q_{entr.} \cdot \frac{1}{2R^2} \cdot \{1 + 2R^2 - \sqrt{1 + 4R^2}\} \text{ with } R = \frac{r}{a} \tag{12}$$

as given in [32] for areas of circular cross section with r the distance of the port axis to the wall (or minor radius of the port), a the distance along the port axis. To

calculate the power flux density towards the port inner surface we balance the reduction of the power fluxes along the port axis $q(a)$ with the fluxes onto a port wall segment for a small da

$$\pi r^2 \cdot (q_\perp(a) - q_\perp(a + da)) = q_{wall} \cdot 2\pi r \cdot da \tag{13}$$

$$\tag{14}$$

as illustrated in figure 15. An expression for the power flux density to the wall is then given by

$$\Rightarrow q_{wall} = -\frac{r}{2} \cdot \frac{q_\perp(a + da) - q_\perp(a)}{da} \tag{15}$$

$$\Rightarrow q_{wall} = -\frac{r}{2} \cdot \frac{\partial q_\perp(a)}{\partial a} \tag{16}$$

and by substituting R and executing the differentiation explicitly we finally get

$$q_{wall} = \frac{r}{4} \cdot q_{entr.} \cdot \left(\left(\frac{a^4}{4r^4} + \frac{a^2}{r^2} \right)^{-\frac{1}{2}} \left(\frac{a^3}{r^4} + \frac{2a}{r^2} \right) - \frac{2a}{r^2} \right) \tag{17}$$

as used for the green curve in figure 13 for the AEX port and AEE port. The latter port must be described with rectangular areas leading to somewhat different analytical expressions, which can also be found in [32] obtained by leaving out the bellow structures as mentioned already earlier.

We get the analytical value for q_{cover} for port AEX by using equation 12 and inserting $a_c = 1.69m$ for the distance between the port entrance and cover plate along the port axis and $r_c = 0.07m$ as the port radius to get $R_{c,AEX} = \frac{r_c}{a_c} = 0.0414$. With this we calculate by assuming that the reflection inside the port is negligible.

$$q_{\perp}(a_c) \quad = q_{entr.} \cdot \frac{1}{2R_{c,AEX}^2} \cdot \{1 + 2R_{c,AEX}^2 - \sqrt{1 + 4R_{c,AEX}^2}\} \tag{18}$$

$$\Rightarrow q_{\perp}(a_c) = q_{entr.} \cdot 0.0017 = 0.084 kW m^{-2} \tag{19}$$

and get the deposited power on the port cover

$$P_{cover} = A_{cover} \cdot q_{\perp}(a_c) = \pi \cdot r_c^2 \cdot 0.084 kW m^{-2} = 13W. \tag{20}$$

We have used the AEX and AEE ports for the analytical description since the port axis points directly to the plasma axis (the description of the axis is presented in equation 11 in section 2.4). In general, the port axis does not point to the plasma axis and so the different assumptions of the radiation distribution plays a larger role. However, it is the aim of the paper to benchmark the numerical results for those cases where an analytical description is simple to compare. For more complex geometries and orientations of the parts which are under investigation, we focus on the numerical results and do not intend to develop a more complex analytical description.

4.4. Local heat loads on Thomson-scattering entrance windows

For the next section, where we will investigate the effect of shielding for the Thomson-scattering windows, we extend our studies again on all five cases and identify the result gained with the worst case for the particular position of the Thomson-scattering ports (AEN & AEM).

As shown in Figure 16 two windows are used for the Thomson-scattering diagnostic, which are embedded in the ports AEN and AEM. The two windows are normally oriented to the port axis. Both windows face a relatively high plasma radiation due to their orientation and size. To assess the necessary cooling of the ports the local heat fluxes on the window surfaces are calculated. We use all five discussed cases and check

moreover, how the smooth radiation profiles of the cases 4 and 5 can be substituted by a weighted combination of the three artificial radiators (cases 1,2,3). We repeat the calculation then for the windows but introduce a shielding that reduces the incoming photon fluxes into the ports but does not restrict viewing access of the diagnostic into the plasma. This shielding is identical to the water cooled steel panels covering the inner wall [1]. The outer shape of the shielding (see Figure 16, right, small boxes at bottom) is due to the CAD representation of the inner wall elements. For our studies only the inner aperture is of importance.

This benchmark is somewhat different than the consideration on the worst case scenario, since the windows are embedded deep in the ports. In general, not only the local heat flux on the idealised wall defines a worst case, but also the effect of the single traces of all photons going into the port relativ to the port axis.

In Table 3 all results are summarised for the studies of the local heat fluxes onto the Thomson-scattering windows. Due to the comparably low number of finite-elements for the shielding, inner wall and windows, very good statistics are achieved (by using more than 50.000.000 photons). The variation of the heat flux density on the window is around 1-2$\frac{kW}{m^2}$. The local values are somewhat larger in the centre of the window and reduced at the edges. The geometrical reduction of the aperture is exactly 50%.

The centrally peaked radiators (case (1) and (4)) cause the largest local heat flux density. The effect of the reduction of the aperture depends only slightly on the chosen radiation profile, which supports the validity of our earlier assumptions that a worst case scenario is mainly dependent on the location on the inner wall.

We find different valuable information from these considerations. First we see that the shielding works better for window 1 with about 66% for the realistic case(4) and

case(5) and has a reduced effect for window 2 with about 44%. Interestingly we find that the shielding works best for case (2) for both windows and almost the same for the cases (1) and (3). However, the differences between the results e.g. for case (1) and case (2) are comparably small. Finally we see that the weighted combination of case(1), case(2) and case(3) reproduce the realistic profiles with negligible deviations. The single weights are gained by taking the local value of the radiation distribution for $\sigma(\rho) = 1 - \rho^2$ and inserting $\rho = 0.05$ for the weight of case(1), $\rho = 0.50$ for case(2) and $\rho = 0.95$ for case(3).

5. Extension to non-poloidal symmetric radiation distribution

The high density divertor operation (HDH-Mode) in W7-AS revealed carbon radiation emission distribution, which is not poloidal symmetric [21] [27]. The observed MARFE-like radiation zones are preferentially located close to the X-Points of the magnetic boundary islands; these regions have been presented in Figure 2 (c) and are also illustrated in Figure 17. It is one of the experimental milestones for W-7X to develope plasma scenarios with similar edge plasma properties (and confinement) as realised with the HDH-Mode in W7-AS.

In order to calculate the radiated power fluxes to the first wall components for such cases, the code has been extended to handle also any non-poloidal symmetric radiation power distribution. Generally, due to its Monte-Carlo based calculation method, any three dimensional radiation distribution, e.g. a non-toroidal symmetric radiator, can be realised. An example model (named case (6) for convenience) suitable to approximate fairly well the radiation distribution following the field lines of the X-Point regions, is to launch test photons in a small circular region within a narrow tube with 20mm

diameter following the X-Point field line. These 5 X-Point lines have a helical structure in stellarator (white dots in Figure 17).

A fully realistic emission distribution may taken in future from sophisticated edge plasma computation as for instance from calculations of the EMC3-EIRENE code package (see e.g. [33]). Based on the experience in W7-AS, it is expected that the radiated power will arise from a wider region as approximated with the narrow tubes of 20mm diameter around the field lines manifesting the X-Point regions. However, the assumed case (6) describes in that respect the upper limit for the peaking factor of the local radiation heat load on the first wall. A widerly extended radiation volume, hence closer to the observation made in W7-AS, will lead to a lower peaking of the radiation heat load on the first wall components.

Figure 18 shows the resulting radiation heat flux onto the vessel wall of case (6), normalised to 10MW total radiated power. For case (6) a maximum value of $90\frac{kW}{m^2}$ is found where for the poloidally symmetric pure edge radiator in case (3) a maximum peak heat fluxes of around 60 $\frac{kW}{m^2}$ has been found.

In order to compare the local heat fluxes of case (6) with the poloidal symmetric case (3), Figure 19 presents the ratio, Δ, between these local heat fluxes:

$$\Delta(\Phi_\oslash, \Theta_\oslash) = \frac{q_{Case(6)}(\Phi_\oslash, \Theta_\oslash)}{q_{Case(3)}(\Phi_\oslash, \Theta_\oslash)}$$

A valuable aspect gained by this simple comparison should be noted by the reader. Depending on the exact position of the ports, the local heat flux is up to factor of 2.4 larger or about two times lower than for the poloidal symmetric radiation model as it can be verified in Figure 19.

W7-X can be operated with 4,5 and 6 boundary islands. The number of the regions with an increased heat load on the inner vessel wall will change their pattern accordingly

to this number. Although the pure X-point radiation scenario is unlikely to occur in real plasma, it gives design values for the maximum heat flux resistance of plasma facing components.

6. Outlook

The calculations of radiated power demonstrate that the remote end of the diagnostic ports (as seen from the plasma axis) receive a very low heat load. The statistical error bars of the heat load on these tiles are largest due to the nature of the applied numerical (Monte-Carlo) method. The heat load itself onto these tiles is small compared to the diagnostic parts which are positioned closer to the plasma. However, for calculation of e.g. thermally induced stresses the gradients must be taken into account and not the local heat fluxes. This makes it necessary to improve the accuracy of even these most remote or shaded regions. Therefore, a photon back tracing method is considered to be implemented in future. This procedure will start a sufficient amount of photon to back trace their paths from the lowest heated areas to the plasma radiation source.

First results have been presented based on non-poloidally symmetric radiation profiles. The feasibility of the code to handle any three dimensional structure, not necessarily following flux surfaces or single field lines, allows to have a general interface with the results of sophisticated transport codes.

The code is fully 3D both for the plasma radiation source as well as the plasma wall. There are no restrictions on the complexity of the considered details of diagnostic, heating ports etc. The input/output data exchanges is already optimised for the ANSYS-FEM solver package. Therefore, the code is certainly applicable for other running or planned fusion experiments like ITER. The latter device has, as a tokamak,

a quasi axisymmetric plasma and within this radiation profiles. The first wall and first wall elements are nevertheless fully 3D and the steady state or long term operation will require a sophisticated heat load assessment.

7. Acknowledgements

The authors are grateful for help and discussion with M.Schubert, P.Grigull, K.McCormick, L.Giannone, T.Klinger, R.Burhenn and B.Streibl.

8. References

[1] M. Wanner, et al., Nucl. Fusion 43 (2003) 416–424.
[2] F. Gadelmeier, et al., Plas.Phys.Contr.Fusion 46 (2004) 711–721.
[3] A. Herrmann, et al., J.Nucl.Mater. 313-316 (2003) 759.
[4] D. Sharma, et al., Nuclear Fusion 45 (2005) 825–836.
[5] R. Dux, et al., J.Nucl.Mater. 337-339 (2005) 852–856.
[6] ANSYS, http://www.ansys.com (2007).
[7] Y. Feng, et al., Plas.Phys.Contr.Fusion 44 (2002) 611–625.
[8] J. Riemann, et al., J.Nucl.Mater. 337-339 (2005) 357–360.
[9] D. Reiter, et al., J.Nucl.Mater. 313-316 (2003) 845–851.
[10] F. Sardei, et al., J.Nucl.Mater. 241-243 (1997) 135–148.
[11] J. Rapp, et al., Plas.Phys.Contr.Fusion 44 (2002) 639–652.
[12] P. Grigull, et al., J.Nucl.Mater. 313-316 (2003) 1287–1291.
[13] R. König, et al., Plas.Phys.Contr.Fusion 44 (2002) 2365–2422.
[14] E. Strumberger, Nuclear Fusion 37 (1997) 19–27.
[15] J. Kisslinger, et al., 'Island Divertors for Helical Devices' in Contributions to 21th Conference on Controlled Fusion and Plasma Physics, Vol. 18B, Part I, Montpellier (1994).
[16] F. Sardei, et al., Contr.Plas.Phys. 34 (1994) 113–119.
[17] T. Eich, et al., Nuclear Fusion 40 (1) (2000) 1757–1772.
[18] F. Nguyen, et al., Nuclear Fusion 37 (1).
[19] E. Strumberger, Nuclear Fusion 36 (1996) 891–908.
[20] J. Samson, Wiley, New York, NY, 1967.
[21] K. McCormick, et al., Phys.Rev.Letter 89 (2002) 015001.
[22] R. Jaenicke, et al., Plas.Phys.Contr.Fusion 44 (2002) B193.
[23] L. Giannone, et al., Plasma Physics and Controlled Fusion 45 (2003) 1713–1731.
[24] L. Giannone, et al., Plasma Physics and Controlled Fusion 44 (2002) 2149–2165.
[25] G. F. Matthews, et al., Nuclear Fusion 39 (1) (1999) 19–40.
[26] A. Kallenbach, et al., Nuclear Fusion 35 (1995) 1231–1246.
[27] U. Wenzel, et al., J.Nucl.Mater. 337-339 (2005) 196–200.
[28] U. Wenzel, et al., Plasma Physics and Controlled Fusion 44 (2002) L57–L62.
[29] E. Strumberger, Nuclear Fusion 40 (2000) 1697–1713.
[30] A. Herrmann, et al., J.Nucl.Mater. 337-339 (2005) 697–701.
[31] F. Schauer, B. Streibl, internal IPP-Report.
[32] VDI, Springer, Berlin, Germany (1997) Kb5.
[33] D. Sharma, et al., Nuclear Fusion 46 (2006) S127–S138.

Table 1. A variety of vacuum fields can be applied for the W7-X stellarator. In this study we focus on the *standard* vacuum field given by the presented coil current distribution. Coils 1-5 are the non-planar coils generating the vacuum field and coils A,B denote the planar coils which are used for the plasma positioning and adjustment of the rotational transform (see figure 1). The coil current is chosen for a magnetic field strength of 2.5T on the axis.

Coil	1	2	3	4	5	A	B	Case
Current[A]	13513	13513	13513	13513	13513	0	0	Standard

Table 2. Overview of the radiation heat load values at several positions along the inner port surface for a subset of all ports of one half module for various radiation profiles. The chosen positions correspond to the boundaries between regions of different cooling capacity as shown in Fig.12.

Case	Port	$q_{\perp}$	q_{P1}^{max}	q_{P1}	q_{P2}	q_{P3}	q_{P4}	q_{cover}	P_{port}	P_{cover}
-	-	$\frac{kW}{m^2}$	$\frac{kW}{m^2}$	$\frac{kW}{m^2}$	$\frac{kW}{m^2}$	$\frac{kW}{m^2}$	$\frac{kW}{m^2}$	$\frac{kW}{m^2}$	kW	kW
1	AEE	70.6	47.6	43.3	34.4	5.0	1.6	1.8	31.4	1.6
1	AEK	62.6	48.6	46.3	29.2	4.4	0.9	1.7	18.7	0.9
1	AEL	72.5	64.9	58.6	24.7	2.3	2.0	1.8	8.0	0.4
1	AEM	51.4	33.8	33.2	17.3	2.1	1.1	2.1	6.2	0.4
1	AET	37.0	24.1	12.3	13.8	1.6	0.4	1.7	4.9	0.4
1	AEV	60.4	38.7	21.0	4.4	0.5	0.5	1.0	1.9	0.1
1	AEX	48.9	27.2	18.8	0.6	0.6	0.5	0.1	0.4	0.1
2	AEE	57.6	43.2	34.7	29.2	4.2	1.5	1.6	26.8	1.7
2	AEK	57.9	40.1	38.0	25.3	3.9	0.9	1.4	17.1	0.7
2	AEL	60.1	59.8	52.1	24.2	1.5	1.2	1.3	7.7	0.3
2	AEM	49.7	35.5	34.1	17.0	1.9	0.9	1.0	6.5	0.2
2	AET	39.0	24.7	15.5	15.6	1.8	0.5	1.4	5.4	0.3
2	AEV	58.0	37.4	26.3	5.1	0.8	0.8	0.3	2.0	0.1
2	AEX	50.9	28.6	22.1	0.7	0.6	0.6	0.1	0.5	0.1
3	AEE	47.6	38.4	28.7	23.8	3.3	1.1	1.1	21.0	0.9
3	AEK	47.8	33.7	30.7	20.5	3.0	0.7	0.8	14.1	0.4
3	AEL	48.0	44.8	24.1	21.2	0.6	0.5	0.2	5.1	0.1
3	AEM	48.6	28.5	27.5	12.0	0.5	0.3	0.4	3.8	0.1
3	AET	45.1	28.0	27.0	18.1	1.9	0.4	0.8	6.2	0.2
3	AEV	53.1	41.6	35.2	4.5	0.5	0.5	0.1	1.9	0.1
3	AEX	53.8	37.4	29.2	0.8	0.8	0.8	0.1	0.6	0.1
4	AEE	66.8	48.5	39.6	25.9	3.7	1.4	1.9	29.2	1.4
4	AEK	64.1	42.9	41.8	25.7	3.7	0.8	1.6	17.7	0.9
4	AEL	65.5	64.0	56.2	29.0	-	1.4	0.4	7.7	0.1
4	AEM	50.7	38.1	36.4	16.2	1.6	0.9	1.2	6.6	0.3
4	AET	37.7	25.9	17.1	14.8	1.6	0.7	2.4	6.0	0.5
4	AEV	59.3	47.8	36.2	3.4	0.6	0.6	0.5	2.1	0.1
4	AEX	49.3	33.0	24.4	3.7	0.1	0.1	0.6	1.3	0.1
analyt.	AEE	66.8	33.4	33.4	15.4	3.2	2.4	3.1	-	1.3
analyt.	AEX	49.3	24.7	21.1	1.4	0.1	0.1	0.084	-	0.0013
5	AEE	52.9	40.1	32.1	26.6	3.7	1.2	1.4	24.0	1.3
5	AEK	52.4	36.5	33.7	22.1	3.5	0.7	1.0	15.2	0.5
5	AEL	52.5	52.8	49.8	23.1	1.2	0.9	1.2	7.2	0.2
5	AEM	49.3	40.0	39.6	18.2	1.5	0.8	0.9	6.6	0.2
5	AET	42.7	28.7	21.5	18.1	1.8	0.4	1.1	6.1	0.2
5	AEV	54.3	39.5	27.7	5.0	0.5	0.5	0.4	2.0	0.1
5	AEX	50.8	33.6	26.1	0.6	0.6	0.6	0.1	0.5	0.1

Table 3. Local heat fluxes on the Thomson scattering laser system entrance windows for all 5 cases. The statistical variation of the error bars is around 0.05-0.2$\frac{kW}{m^2}$. The values for cases (4*,5*) are gained by a weighted combination of the artificial profiles (1,2,3). The effect of the reduction (Red.) of the aperture is given in percentage. Larger number means better shielding.

Case		Window 1 no shield	Window 1 with shield	Red. %	Window 2 no shield	Window 2 with shield	Red. %
		$\frac{kW}{m^2}$	$\frac{kW}{m^2}$		$\frac{kW}{m^2}$	$\frac{kW}{m^2}$	
1	$0.00 \leq \rho \leq 0.10$	21.97	8.81	59.9	11.56	6.76	41.5
2	$0.45 \leq \rho \leq 0.55$	20.20	6.35	68.8	12.92	6.25	51.6
3	$0.90 \leq \rho \leq 1.00$	13.64	5.43	60.2	8.90	5.17	41.9
4	centrally peaked	19.94	6.85	65.6	11.29	6.08	46.2
4*	case 4 interpol	20.44	7.51	63.3	11.81	6.40	45.8
5	add. edge rad.	17.52	5.69	67.5	9.98	5.94	40.5
5*	case 5 interpol	15.44	5.98	61.3	9.67	5.5	43.1

9. Figure captions

9.1. Figure 1

Overview of the Wendelstein-7X plasma wall and superconducting coils. Note the 5 non-planar (coil 1,2,3,4,5) and the 2 planar (coil A,B) coils of each half-module. For the complete torus 10 half-modules are combined resulting in a fivefold symmetry. About 300 ports are used for heating, supply and diagnostical access to the plasma.

9.2. Figure 2

Poincaréplots of the magnetic equilibrium field (one half module) for (a) $\Phi = 0$,(b) $\pi/15$,(c) $\pi/10$ and (d) $\pi/5$. The normalised magnetic radial axis ranges from the plasma axis at $\rho = 0$ to the LCFS at $\rho = 1$. The plane at $\Phi = 0$ is called bean plane and the plane at $\Phi = \pi/5$ is called triangle plane. In Figure (c) additionally the X-Point regions are indicated laying poloidally between the 5 centre of the island chains.

9.3. Figure 3

The distance $r_{\oslash}$ of the closed (idealised) plasma wall from the plasma axis defined by R_{axis} and z_{axis} presented for one of the five modules from $\Phi = -\pi/5$ to $+\pi/5$. Note the strong variation of $r_{\oslash}$ resembling the helicity of the W-7X experiment. The white checkered regions mark the position of the divertor target plates (HHF-components) which are designed to receive very large (convective) heat loads but are not of interest for this paper.

9.4. Figure 4

Five different cases of radiation profiles are studied. Three cases of artifical radiation distribution (1,2,3) and two further cases assumed to describe (4) emission proportional

to the square of the minor radius and (5) emission proportional to the square of the minor radius with additional line radiation from impurities in the very edge region.

9.5. Figure 5

Heat load distribution for pure (artificial) central radiation with $\sigma(\rho) = 1$ for $0 \leq \rho \leq 0.1$. Note the large variation of the local heat flux densities by a factor of about 13. Different cuts (marked with different line styles) are presented showing the excellent quality of the Monte-Carlo based results.

9.6. Figure 6

Heat load distribution for a pure (artificial) belt radiation with $\sigma(\rho) = 1$ for $0.45 \leq \rho \leq 0.55$.

9.7. Figure 7

Heat load distribution for a pure (artificial) edge radiation with $\sigma(\rho) = 1$ for $0.9 \leq \rho \leq 1.0$ Note the reduced local variation of the heat flux densities when compared to pure (artificial) central radiation distribution.

9.8. Figure 8

Heat load distribution for the realistic radiation profile case (5).

9.9. Figure 9

Difference between a linear interpolation of cases (1-3) approximating case (5) and the exact heat distribution for case (5).

9.10. Figure 10

The plasma wall (shown for half module 10) of the W-7X stellarator with 34 diagnostic and heating ports. Each port is embedded in the plasma wall and the outer machine

wall and contains a bellow to allow for the differential expansion and movements of the inner and outer machine wall due to heating/cooling and magnetic forces, respectively. Only those ports are marked for which the heat load calculations are presented. The port of type AEX is longer included in the present design, its shape and orientation, however, is of interest for comparison with analytical models.

9.11. Figure 11

Heat load for the realistic plasma and radiation distribution case (5). Illustrated are a FEM wall representation showing the port opening labelled only for the subset of ports which are described in Table 2.

9.12. Figure 12

Due to the engineering requirements different areas of interest for the cooling capacity assessment are defined. Particularly the four marked positions of the averaged heat flux density values along the port axis (Pos.1-3) and at the transition to the bellow region (Pos.4) are analysed. Additionally the maximum local heat flux density at Pos. 1 (q_{P1}^{max}), that is calculated for three single finite elements with maximum $q_{rad.}$, is presented.

9.13. Figure 13

Comparison of numerically (solid line) and analytically (dashed) calculated radiative heat load onto the inner port surface for port AEX.

9.14. Figure 14

Comparison of numerically (solid line) and analytically (dashed) calculated radiative heat load onto the inner port surface for port AEE.

9.15. Figure 15

Sketch of the geometry and quantities as used for the analytical model for a port with circular cross section receiving photons from a semi-infinite volume of plasma radiation.

9.16. Figure 16

Heat load on the upper part of a half module with the ports and entrance windows of the Thomson-Scattering system for case (4). For clarity a simplified model for the plasma vessel and port structure is chosen. Option (**1**) illustrates the solution with open ports and option (**2**) a solution with shields to reduce the power loading on the Thomson scattering entrance windows without restricting the diagnostical access to the plasma volume.

9.17. Figure 17

A non poloidal symmetric edge radiator is approximated by radiation arising purely from the 5 x-points like lines between the island chain as shown in Figure 2 (c)

9.18. Figure 18

The resulting heat flux density as caused by the non-poloidal symmetric radiation distribution consistent of 5 separated radiation belts follwowing the 5 X-Point region between the magnetic islands (case (6)) as shown in Fig.17 and Figure 2 (c).

9.19. Figure 19

The ratio (Δ) between the local heat fluxes of the non-poloidal symmetric case (6) with 5 radiation belts and the pure edge radiator of case (3).

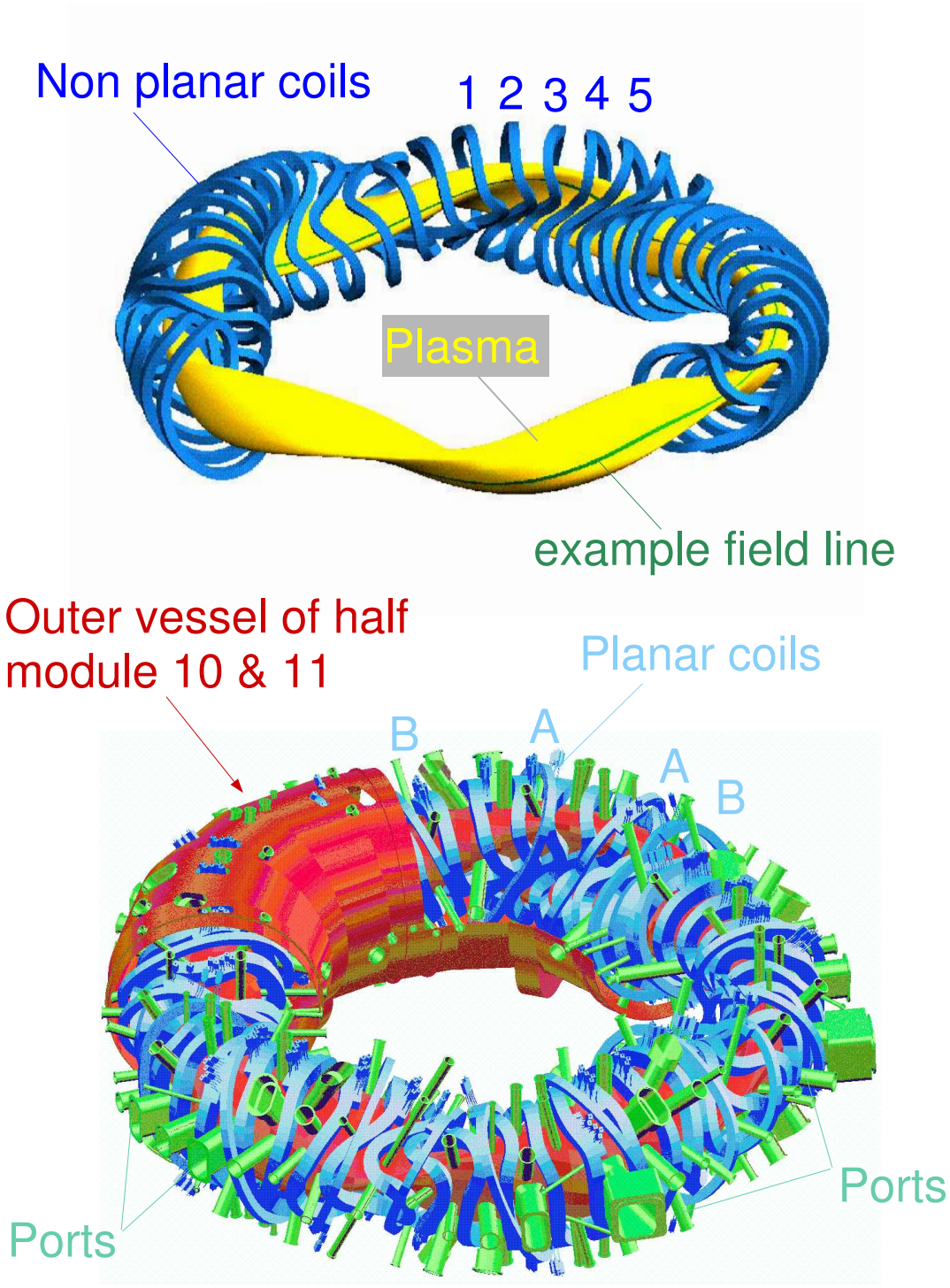
Non planar coils
1 2 3 4 5
Plasma
example field line
Outer vessel of half module 10 & 11
Planar coils
B
A
A
B
Ports
Ports

Figure 1.

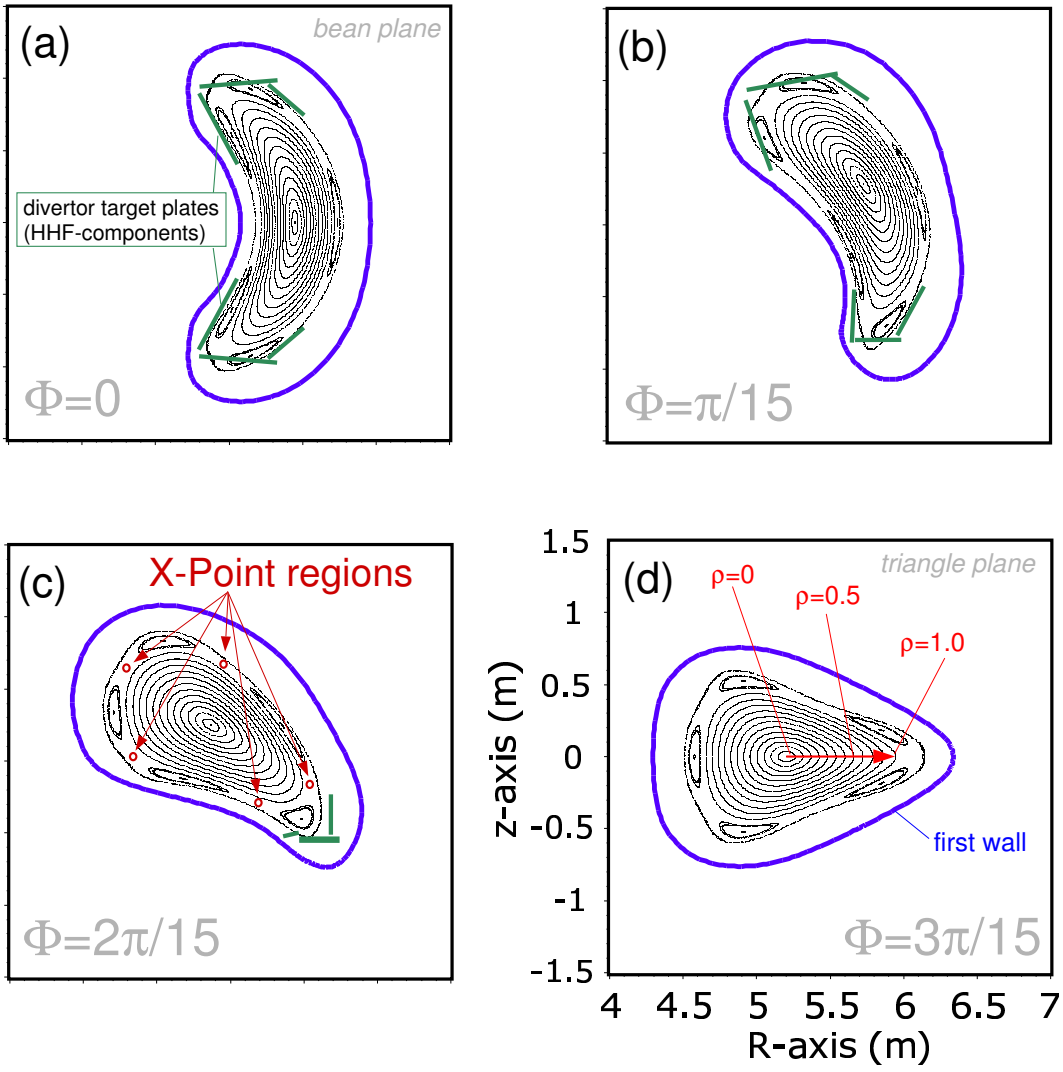
(a)
bean plane
divertor target plates
(HHF-components)
Φ=0
(b)
Φ=π/15
(c)
X-Point regions
Φ=2π/15
(d)
triangle plane
ρ=0
ρ=0.5
ρ=1.0
first wall
Φ=3π/15
z-axis (m)
R-axis (m)
1.5
1
0.5
0
-0.5
-1
-1.5
4
4.5
5
5.5
6
6.5
7

Figure 2.

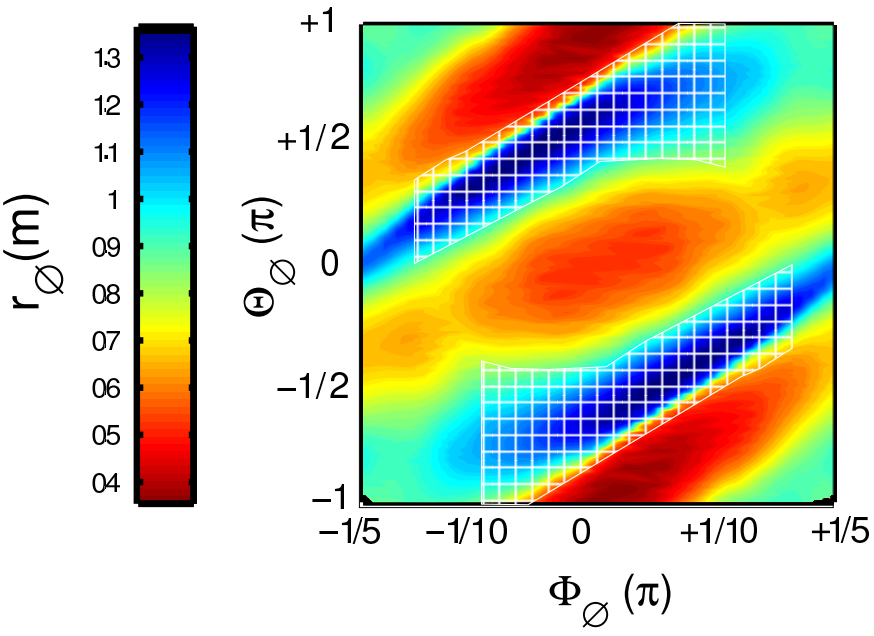

Figure 3.

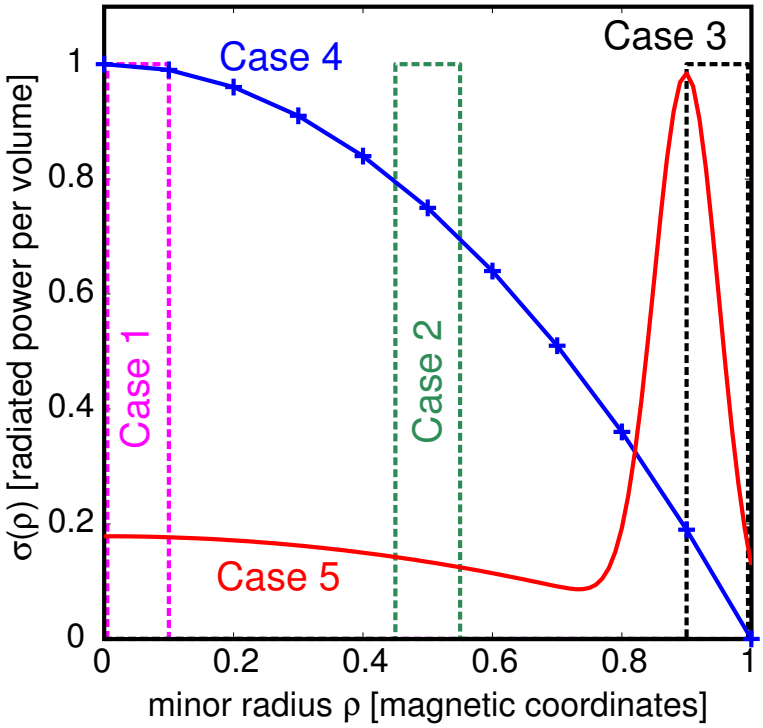
Case 4
Case 3
Case 1
Case 2
Case 5
σ(ρ) [radiated power per volume]
minor radius ρ [magnetic coordinates]
0
0.2
0.4
0.6
0.8
1

Figure 4.

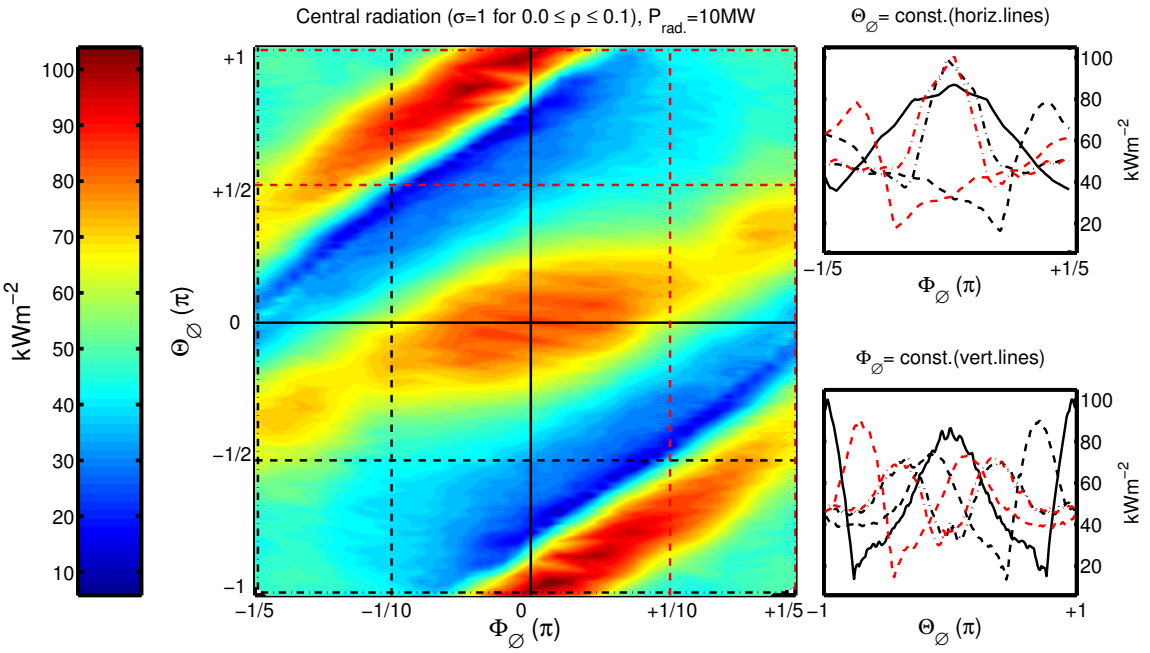
Central radiation (σ=1 for 0.0 ≤ ρ ≤ 0.1), P_rad.=10MW
Θ∅= const.(horiz.lines)
Φ∅= const.(vert.lines)
kWm−2
Θ∅ (π)
Φ∅ (π)
+1
+1/2
0
−1/2
−1
−1/5
−1/10
+1/10
+1/5
100
90
80
70
60
50
40
30
20
10
kWm−2

Figure 5.

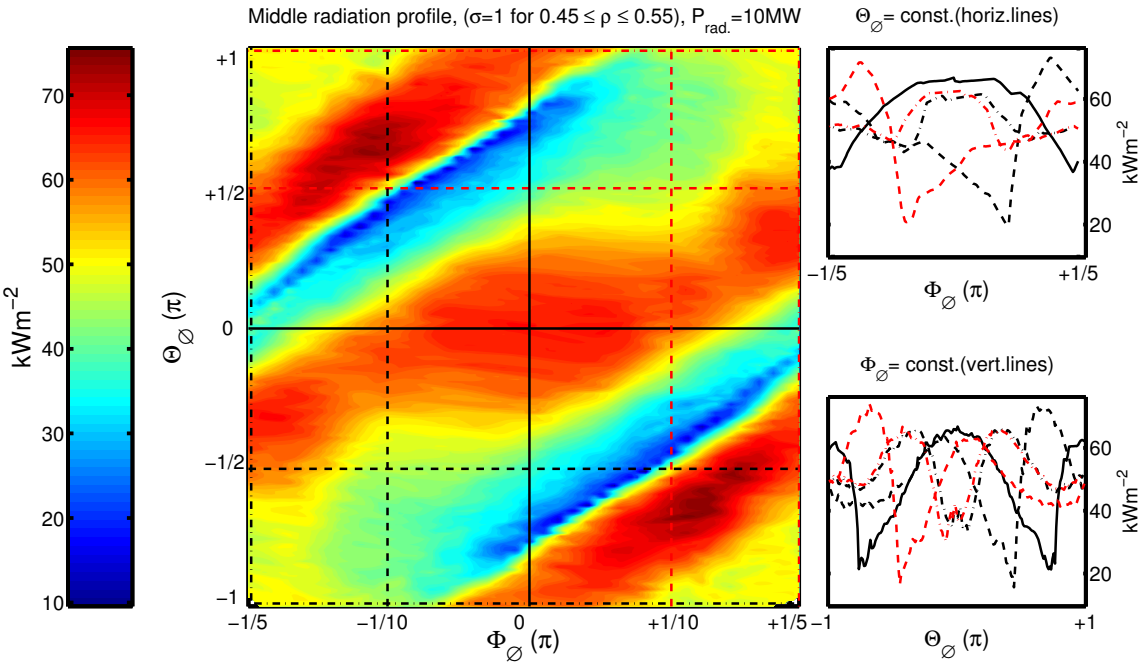
Middle radiation profile, (σ=1 for 0.45 ≤ ρ ≤ 0.55), P rad.=10MW
Θ∅= const.(horiz.lines)
Φ∅= const.(vert.lines)
kWm−2
Θ∅ (π)
Φ∅ (π)
+1
+1/2
0
−1/2
−1
−1/5
−1/10
+1/10
+1/5
70
60
50
40
30
20
10

Figure 6.

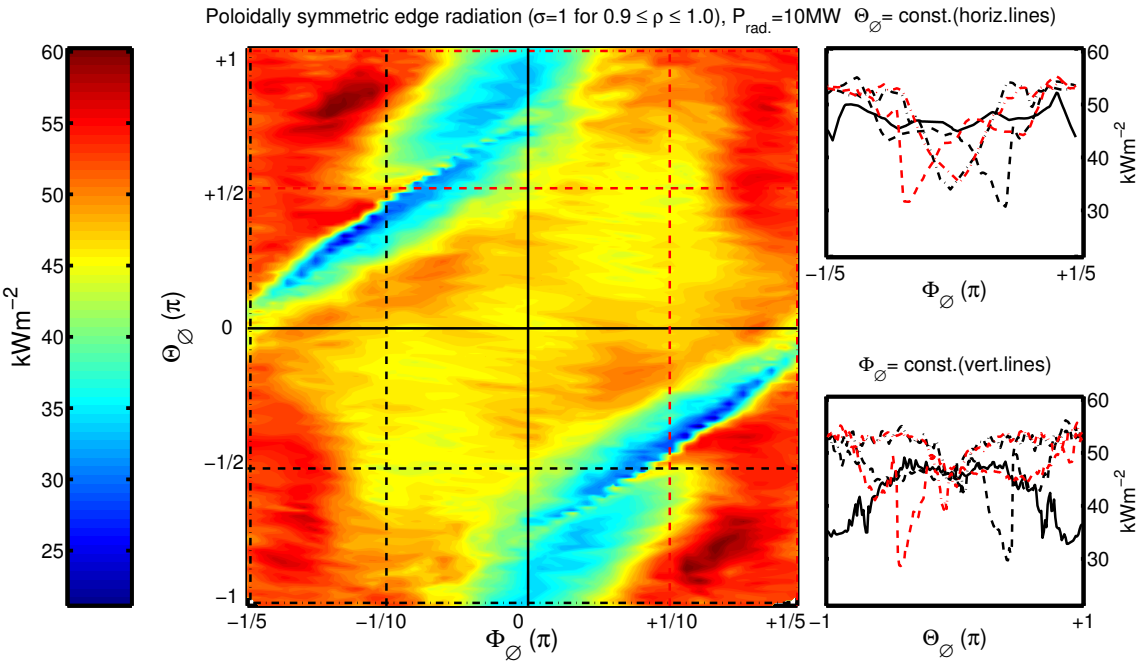
Poloidally symmetric edge radiation (σ=1 for 0.9 ≤ ρ ≤ 1.0), P_rad.=10MW Θ_∅= const.(horiz.lines)
kWm^-2
60
55
50
45
40
35
30
25
Θ_∅ (π)
+1
+1/2
0
−1/2
−1
−1/5
−1/10
0
+1/10
+1/5
Φ_∅ (π)
−1/5
+1/5
Φ_∅ (π)
kWm^-2
60
50
40
30
Φ_∅= const.(vert.lines)
−1
+1
Θ_∅ (π)
kWm^-2
60
50
40
30

Figure 7.

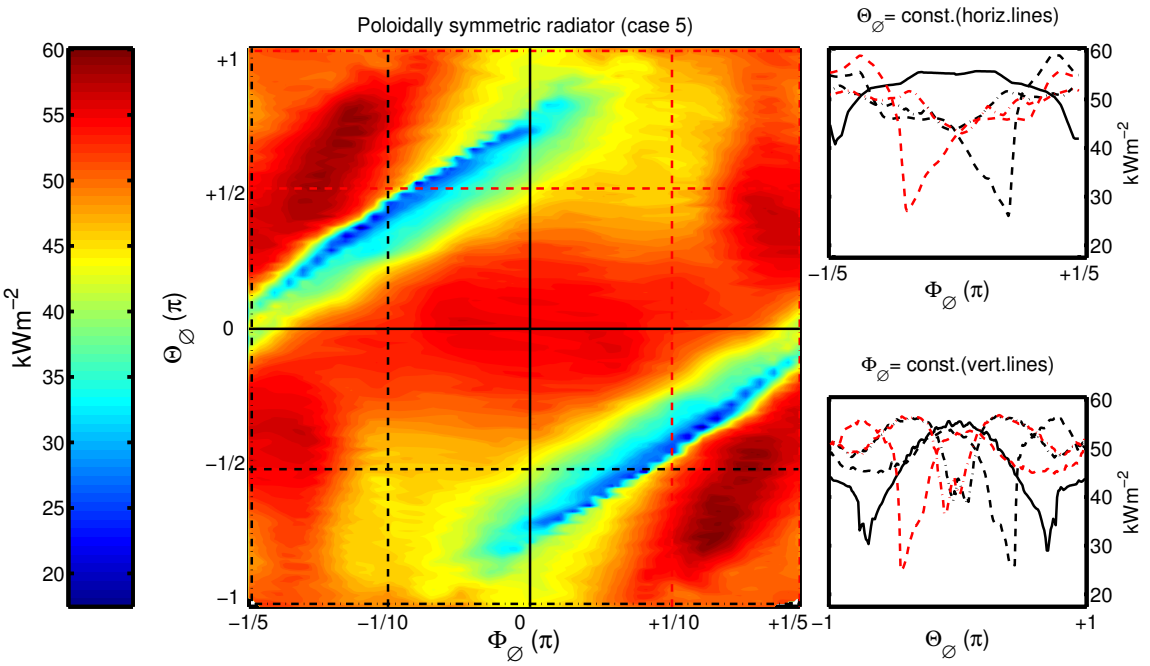
Poloidally symmetric radiator (case 5)
kWm^{-2}
60
55
50
45
40
35
30
25
20
+1
+1/2
0
−1/2
−1
$\Theta_\varnothing$ (π)
−1/5
−1/10
0
+1/10
+1/5
$\Phi_\varnothing$ (π)
$\Theta_\varnothing$= const.(horiz.lines)
$\Phi_\varnothing$ (π)
$\Phi_\varnothing$= const.(vert.lines)
$\Theta_\varnothing$ (π)
−1
+1

Figure 8.

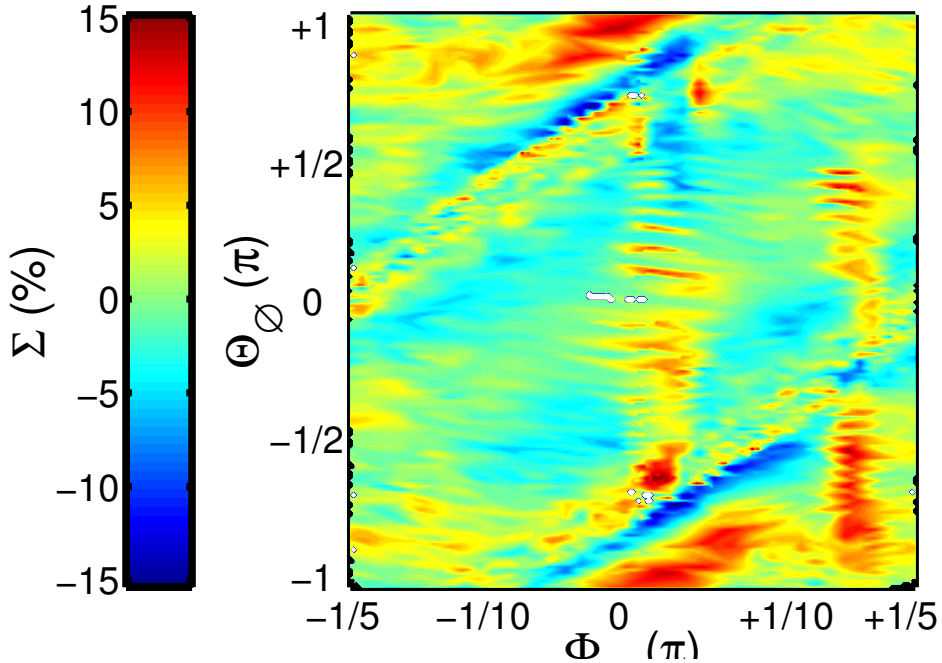

Figure 9.

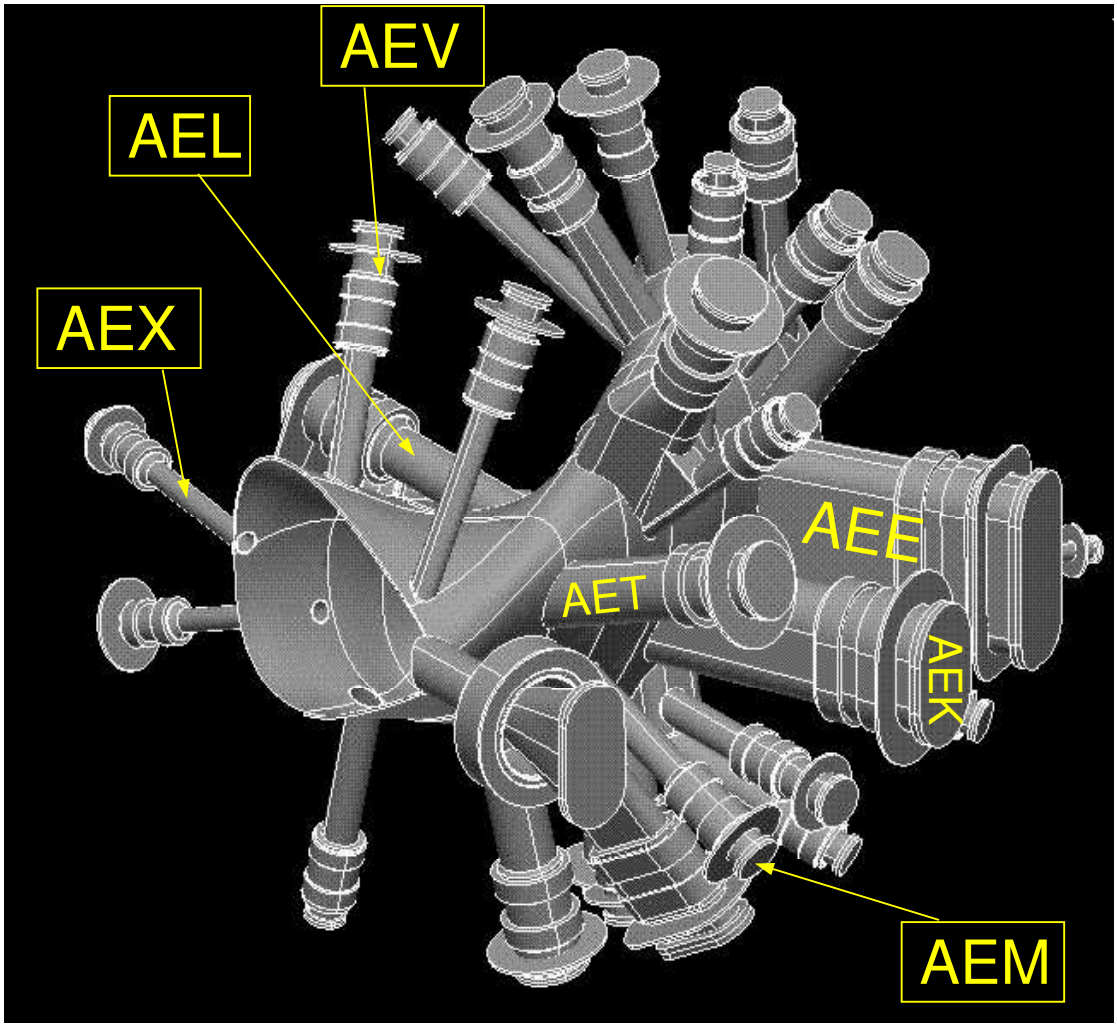

Figure 10.

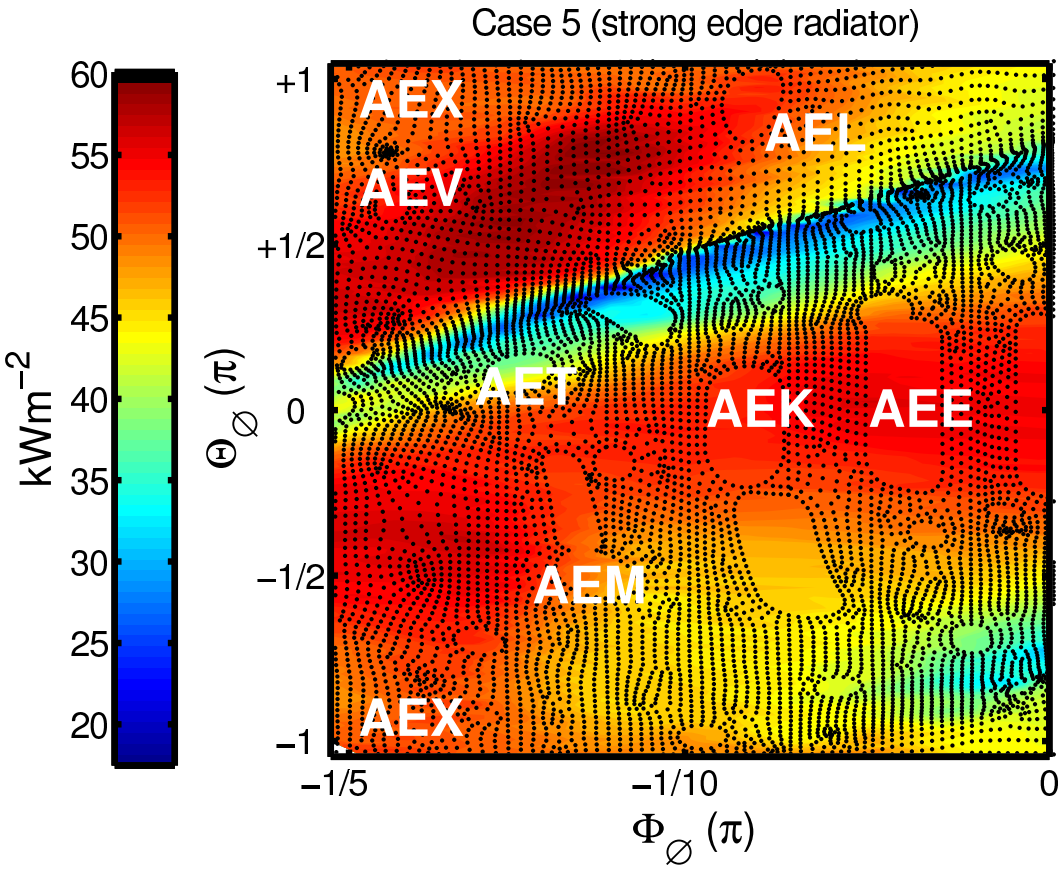
Case 5 (strong edge radiator)
AEX
AEL
AEV
AET
AEK
AEE
AEM
AEX
60
55
50
45
40
35
30
25
20
kWm^{-2}
+1
+1/2
0
−1/2
−1
$\Theta_{\varnothing}$ (π)
−1/5
−1/10
0
$\Phi_{\varnothing}$ (π)

Figure 11.

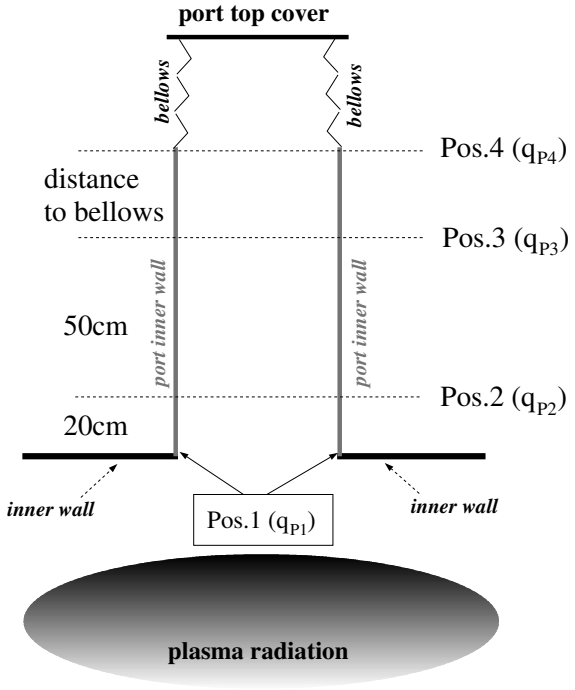
port top cover
bellows
bellows
Pos.4 (q_{P4})
distance
to bellows
Pos.3 (q_{P3})
port inner wall
port inner wall
50cm
Pos.2 (q_{P2})
20cm
inner wall
Pos.1 (q_{P1})
inner wall
plasma radiation

Figure 12.

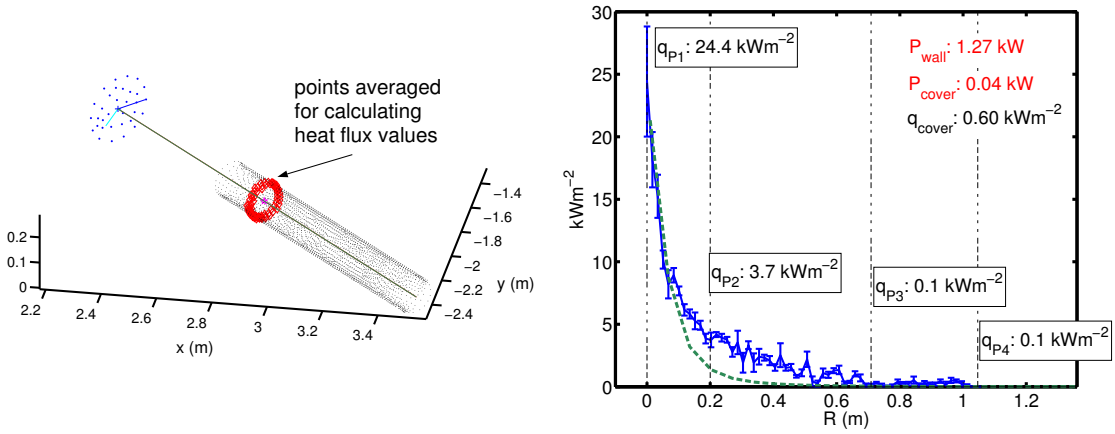
points averaged
for calculating
heat flux values
x (m)
y (m)
kWm^{-2}
R (m)
q_{P1}: 24.4 kWm^{-2}
q_{P2}: 3.7 kWm^{-2}
q_{P3}: 0.1 kWm^{-2}
q_{P4}: 0.1 kWm^{-2}
P_{wall}: 1.27 kW
P_{cover}: 0.04 kW
q_{cover}: 0.60 kWm^{-2}

Figure 13.

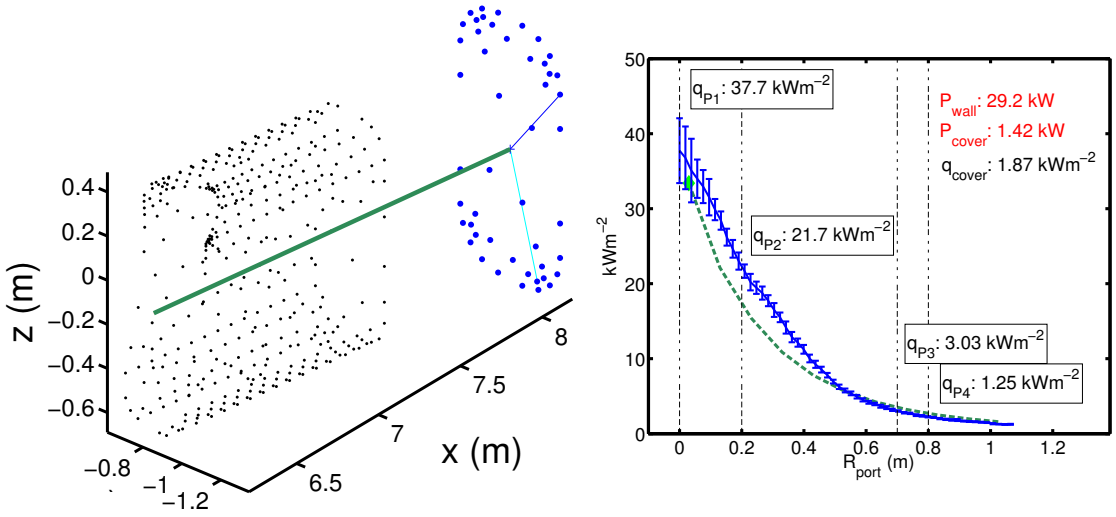
z (m)
0.4
0.2
0
−0.2
−0.4
−0.6
−0.8
−1
−1.2
6.5
7
7.5
8
x (m)
kWm^{-2}
50
40
30
20
10
0
0
0.2
0.4
0.6
0.8
1
1.2
R$_{port}$ (m)
q$_{P1}$: 37.7 kWm^{-2}
q$_{P2}$: 21.7 kWm^{-2}
q$_{P3}$: 3.03 kWm^{-2}
q$_{P4}$: 1.25 kWm^{-2}
P$_{wall}$: 29.2 kW
P$_{cover}$: 1.42 kW
q$_{cover}$: 1.87 kWm^{-2}

Figure 14.

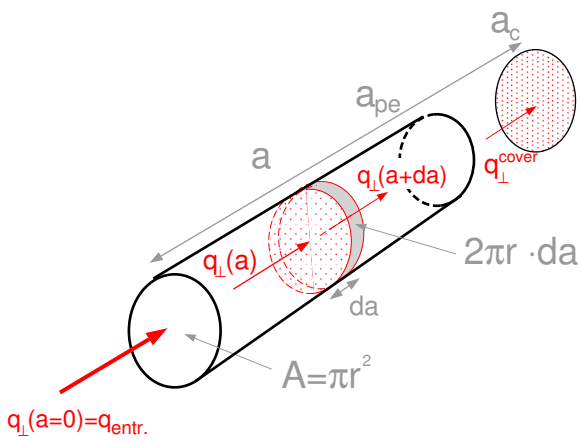

Figure 15.

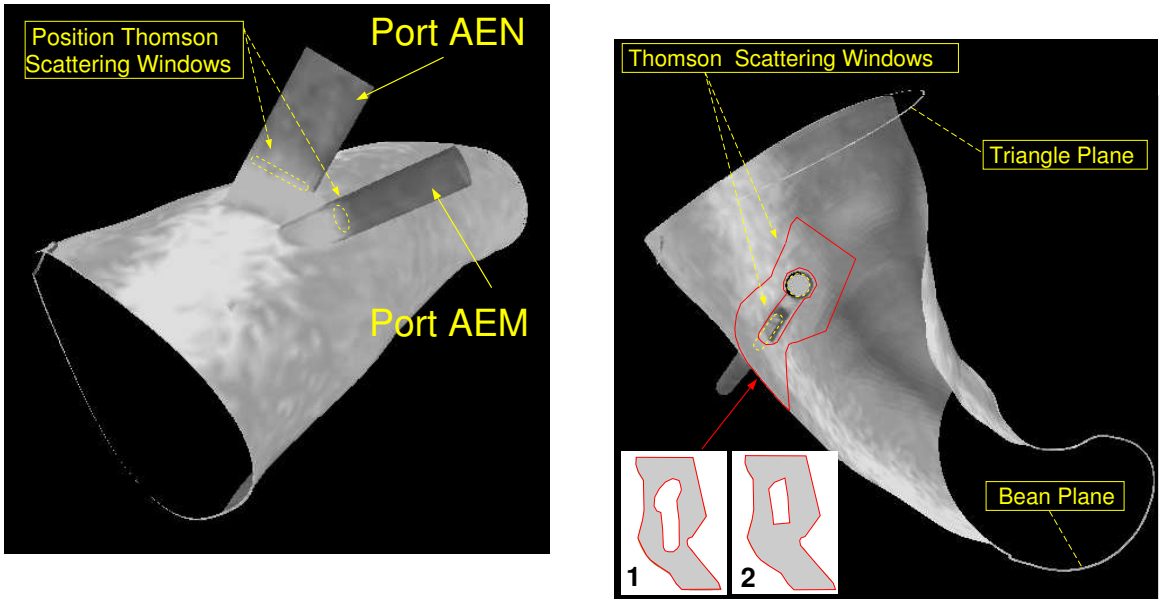
Position Thomson
Scattering Windows
Port AEN
Port AEM
Thomson Scattering Windows
Triangle Plane
Bean Plane
1
2

Figure 16.

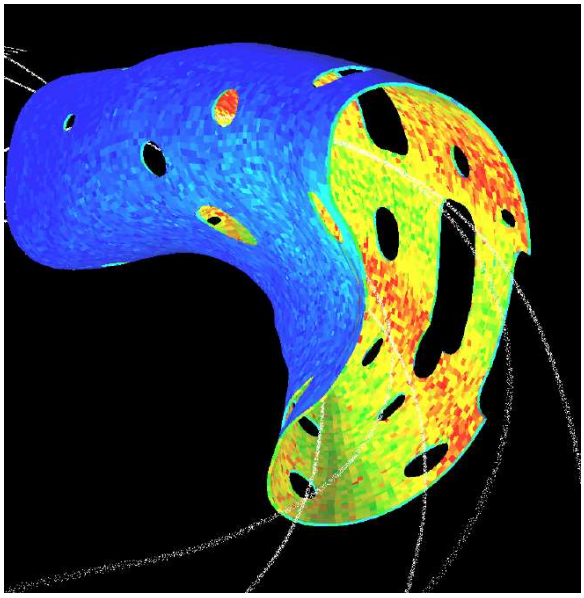

Figure 17.

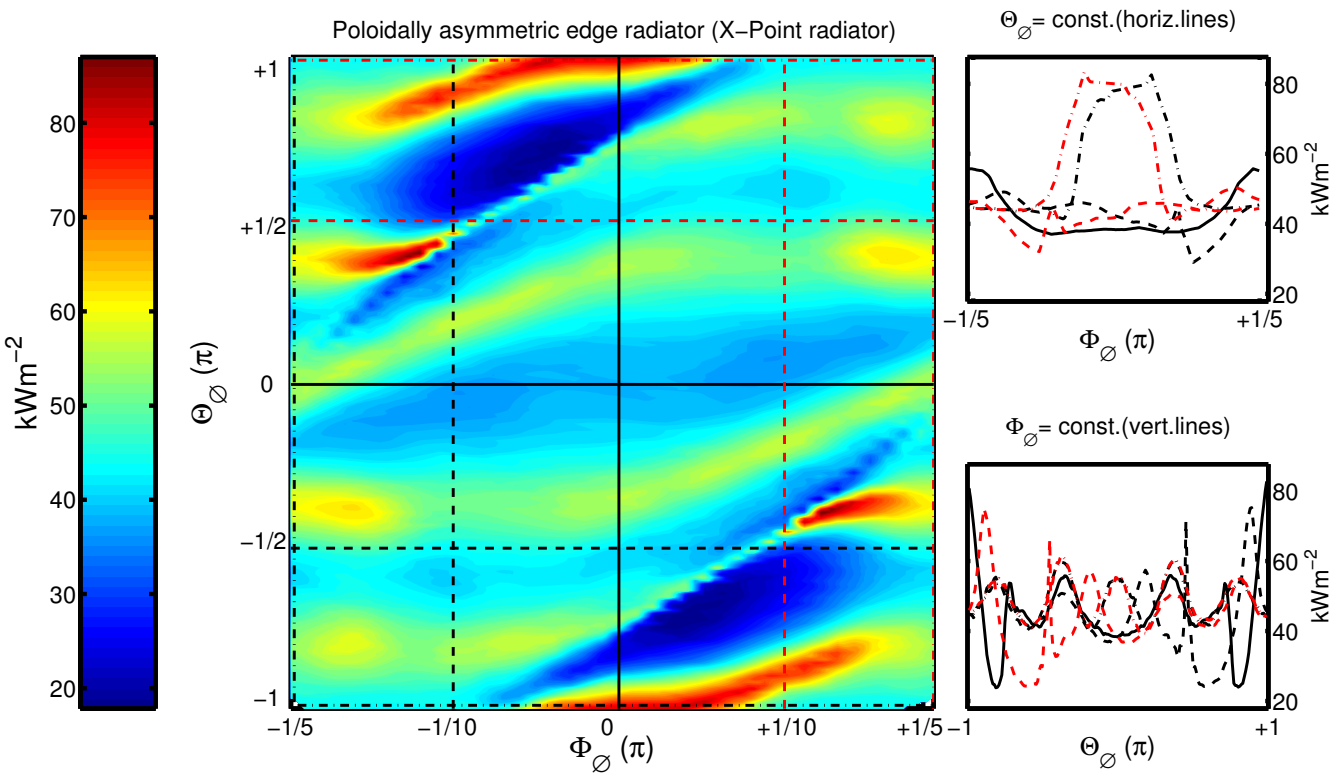
Poloidally asymmetric edge radiator (X–Point radiator)
kWm^{-2}
80
70
60
50
40
30
20
$\Theta_{\varnothing}$ (π)
+1
+1/2
0
−1/2
−1
−1/5
−1/10
0
+1/10
+1/5
$\Phi_{\varnothing}$ (π)
$\Theta_{\varnothing}$= const.(horiz.lines)
80
60
40
20
kWm^{-2}
−1/5
+1/5
$\Phi_{\varnothing}$ (π)
$\Phi_{\varnothing}$= const.(vert.lines)
80
60
40
20
kWm^{-2}
−1
+1
$\Theta_{\varnothing}$ (π)

Figure 18.

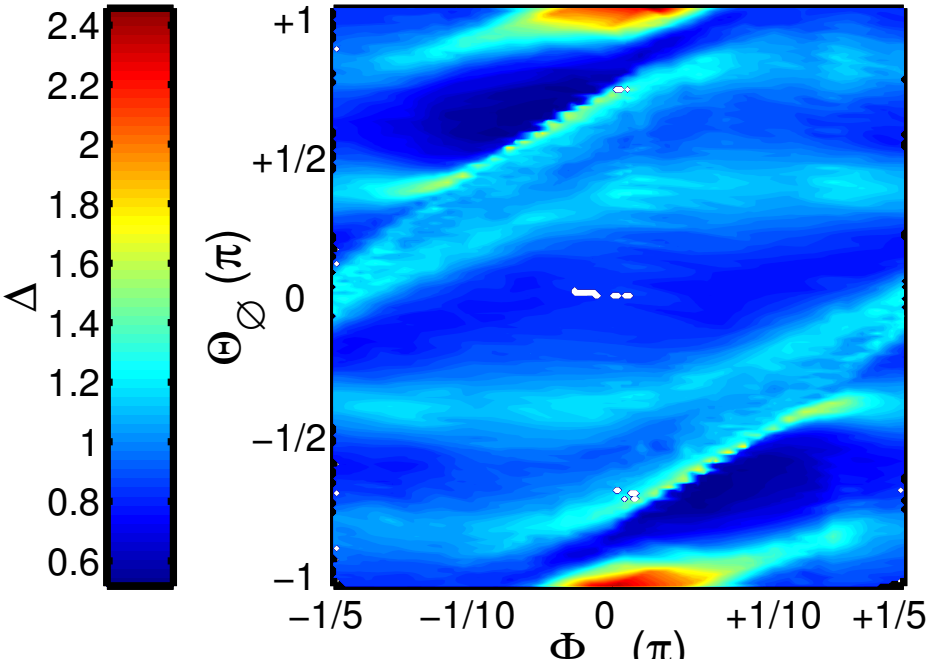

Figure 19.